

A WIDE-FIELD 90 CENTIMETER VLA IMAGE OF THE GALACTIC CENTER REGION

T. N. LAROSA¹

Department of Biological and Physical Sciences, Kennesaw State University, 1000 Chastain Road, Kennesaw, GA 30144; ted@avatar.kennesaw.edu

NAMIR E. KASSIM AND T. JOSEPH W. LAZIO

Remote Sensing Division, Naval Research Laboratory, Code 7213, Washington, DC 20375-5351; kassim@rsd.nrl.navy.mil, lazio@rsd.nrl.navy.mil

AND

S. D. HYMAN

Department of Physics, Sweet Briar College, Sweet Briar, VA 24595; hyman@sbcc.edu

Received 1999 June 28; accepted 1999 September 21

ABSTRACT

We present a wide-field, high dynamic range, high-resolution, long-wavelength ($\lambda = 90$ cm) VLA image of the Galactic center region. The image is centered on Sgr A, covers an area of $4^\circ \times 5^\circ$ with an angular resolution of $43''$, and has a rms sensitivity of ≈ 5 mJy beam⁻¹. The image was constructed from archival (1989 and 1991) VLA data of Pedlar et al. and Anantharamaiah et al. using new three-dimensional image restoration techniques. These three-dimensional imaging techniques resolve the problem of non-coplanar baselines encountered at long wavelengths and yield distortion-free imaging of far-field sources with improved sensitivity. At $\lambda = 90$ cm the VLA is sensitive to both thermal and non-thermal emission and the resulting image gives an unprecedented contextual perspective of the large-scale radio structure in this unique and complicated region. We have catalogued over a hundred sources from this image and present for each source its 90 cm flux density, position, and size. For many of the small-diameter sources, we also derive the 20/90 cm spectral index. The spectral index as a function of length along several of the isolated nonthermal filaments has been estimated and found to be constant. We have found six new small-diameter sources, as well as several extended regions of emission, which are clearly distinct sources that have not been previously identified at higher frequencies. These data are presented as a first epoch of VLA observations that can be used to search for source variability in conjunction with a second epoch of observations that were recently initiated.

Key words: Galaxy: center — radio continuum

1. INTRODUCTION

The Galactic center harbors a number of unique radio sources and structures. Within the central $15'$ ($= 37$ pc for an assumed distance of 8.5 kpc) the most notable of these structures is the Sgr A complex, which consists of the compact synchrotron source Sgr A*, (Balick & Brown 1974; Beckert et al. 1996) about which the thermal spiral Sgr A West (Ekers et al. 1983; Lo & Claussen 1983) appears to be in orbit (Serabyn et al. 1988; Lacy, Achetermann, & Serabyn 1991). Along this same line of sight is Sgr A East, a nonthermal shell source (Ekers et al. 1983) that may be the remnant of an explosive event involving some 40 times the energy of a single supernova explosion (Mezger et al. 1989; Khokhlov & Melia 1996).

Located some $15'$ – $20'$ north of Sgr A (50 pc in projection), the Galactic center radio arc (GCRA) is arguably the most striking radio structure observed in our Galaxy. This structure was first resolved into a large number of narrow linear features by Yusef-Zadeh, Morris, & Chance (1984). These filamentary structures show strong polarization with no line emission and are therefore nonthermal synchrotron sources, most likely magnetic flux tubes filled with relativistic electrons. Several prominent H II regions cross and appear to interact with the GCRA filaments suggesting in situ particle acceleration via magnetic reconnection between a large-scale magnetic field and molecular cloud magnetic fields (e.g., Serabyn & Morris 1994).

In addition to the GCRA filaments there are a number of isolated filaments within the central 0.5° that are also non-thermal magnetic structures (Morris & Yusef-Zadeh 1985; Bally & Yusef-Zadeh 1989; Gray et al. 1991; Anantharamaiah et al. 1991). Of the seven filaments identified, all but one are oriented perpendicular to the Galactic plane (Anantharamaiah et al. 1999; Lang et al. 1999a). These filaments may be locally illuminated flux tubes in a large-scale pervasive field (Uchida et al. 1996; Staguhn et al. 1998) or local enhancements in an otherwise weak magnetic field (e.g., Shore & LaRosa 1999). In the former case they presumably trace the large-scale magnetic field in the GC (Morris 1994). One of the most prominent of these filaments is the Sgr C filament. It is located to the south of Sgr A, about 75 pc in projection, and appears at high resolution to consist of several subfilaments (Liszt 1985; Liszt & Spiker 1995).

On a larger scale the GCRA and the Sgr C filament appear to connect with the legs of a 100–200 pc looplike structure denoted the “Omega lobe” or GC lobe (Sofue & Handa 1984; Sofue 1985). The legs of this feature are strongly polarized, indicating that it is also a magnetic structure (Sofue 1994). Several models for this feature invoke activity in the GC, either direct explosion (Sofue 1985) or MHD acceleration of twisted poloidal magnetic field associated with an accretion disk dynamo (Uchida, Shibata, & Sofue 1985; Uchida & Shibata 1986). Larger scale radio features (e.g., the 4 kpc radio jet, Sofue, Reich, & Reich 1989 and the 2 kpc-scale polarized plume, Duncan et al. 1998) have also been interpreted as evidence for activity at the GC.

¹ Navy-ASEE Summer Faculty Fellow, Naval Research Laboratory.

Report Documentation Page				Form Approved OMB No. 0704-0188	
Public reporting burden for the collection of information is estimated to average 1 hour per response, including the time for reviewing instructions, searching existing data sources, gathering and maintaining the data needed, and completing and reviewing the collection of information. Send comments regarding this burden estimate or any other aspect of this collection of information, including suggestions for reducing this burden, to Washington Headquarters Services, Directorate for Information Operations and Reports, 1215 Jefferson Davis Highway, Suite 1204, Arlington VA 22202-4302. Respondents should be aware that notwithstanding any other provision of law, no person shall be subject to a penalty for failing to comply with a collection of information if it does not display a currently valid OMB control number.					
1. REPORT DATE JAN 2000		2. REPORT TYPE		3. DATES COVERED 00-00-2000 to 00-00-2000	
4. TITLE AND SUBTITLE A Wide-Field 90 Centimeter VLA Image of the Galactic Center Region				5a. CONTRACT NUMBER	
				5b. GRANT NUMBER	
				5c. PROGRAM ELEMENT NUMBER	
6. AUTHOR(S)				5d. PROJECT NUMBER	
				5e. TASK NUMBER	
				5f. WORK UNIT NUMBER	
7. PERFORMING ORGANIZATION NAME(S) AND ADDRESS(ES) Naval Research Laboratory, Code 7213, 4555 Overlook Avenue, SW, Washington, DC, 20375				8. PERFORMING ORGANIZATION REPORT NUMBER	
9. SPONSORING/MONITORING AGENCY NAME(S) AND ADDRESS(ES)				10. SPONSOR/MONITOR'S ACRONYM(S)	
				11. SPONSOR/MONITOR'S REPORT NUMBER(S)	
12. DISTRIBUTION/AVAILABILITY STATEMENT Approved for public release; distribution unlimited					
13. SUPPLEMENTARY NOTES					
14. ABSTRACT					
15. SUBJECT TERMS					
16. SECURITY CLASSIFICATION OF:			17. LIMITATION OF ABSTRACT	18. NUMBER OF PAGES 35	19a. NAME OF RESPONSIBLE PERSON
a. REPORT unclassified	b. ABSTRACT unclassified	c. THIS PAGE unclassified			

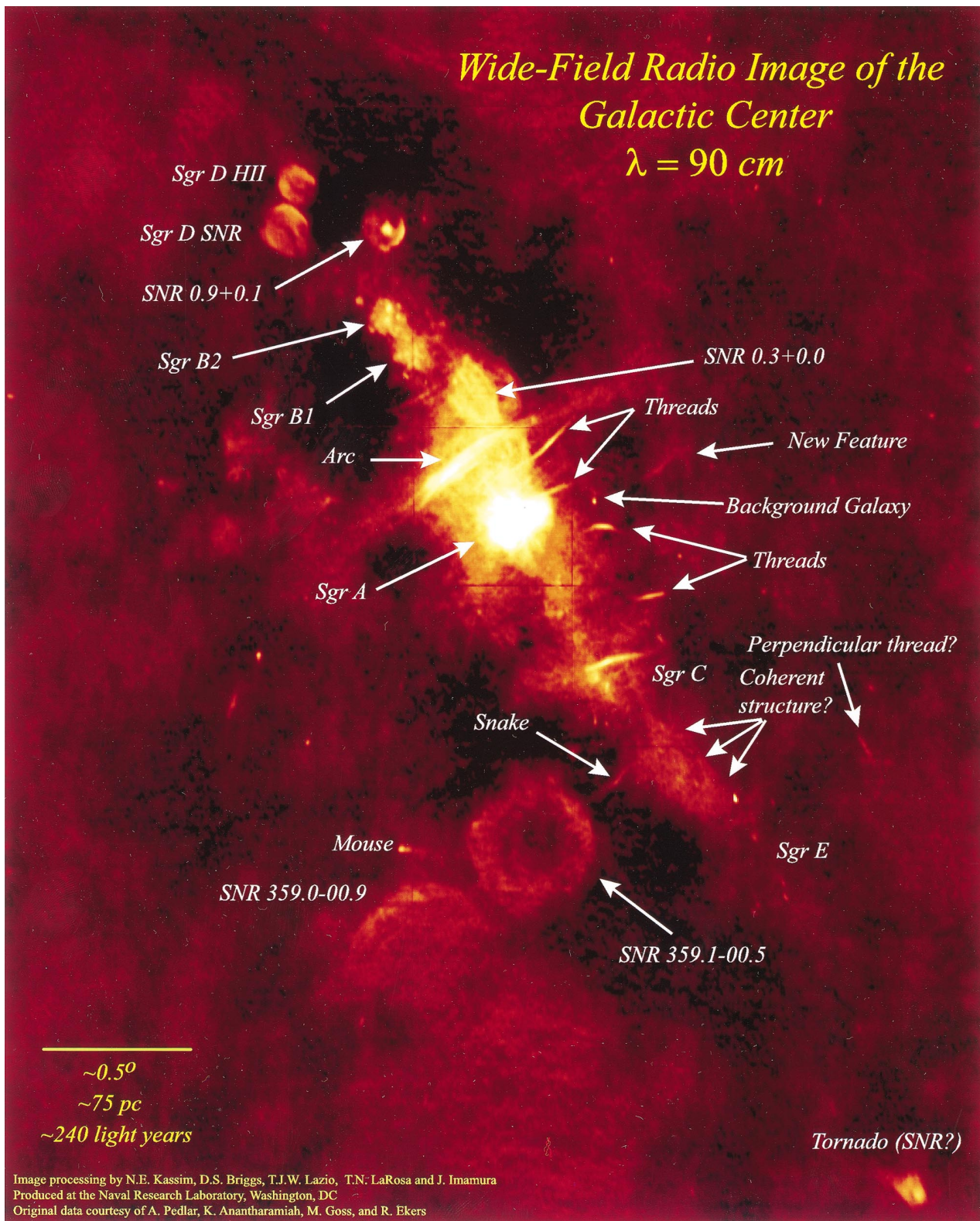


FIG. 1.—Galactic center at 90 cm. This is a $4^\circ \times 2.5'$ subimage with a resolution of $43'' \times 24''$ and an rms sensitivity of 5 mJy beam^{-1} (away from the strong emission on the Galactic ridge).

This radio continuum view, together with millimeter, infrared, and X-ray observations suggest that the center of our Galaxy is a weak, Seyfert-type nucleus driven by a black hole coincident with the compact source Sgr A* (for detailed reviews, see Mezger, Duschl, & Zylka 1996; Morris & Serabyn 1996). While an overall picture of the GC as a

mildly active starburst galaxy is beginning to emerge, the origin and nature of many of the sources discussed above is still very uncertain. Given the wide range in angular scale and intensity of the sources, a deeper understanding of the GC will require sensitive, high-resolution, wide-field observations, combined with detailed theoretical modeling.

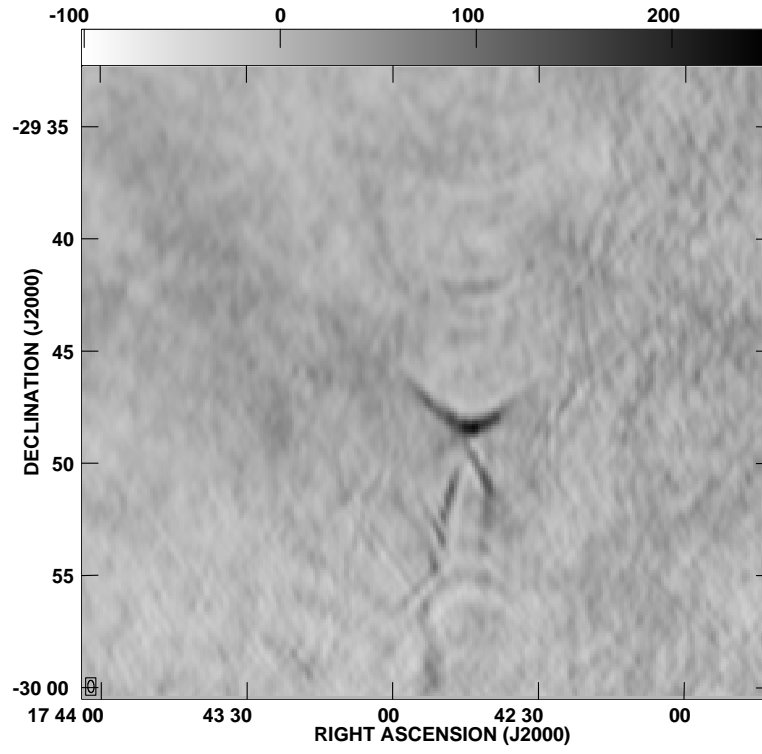


FIG. 3a

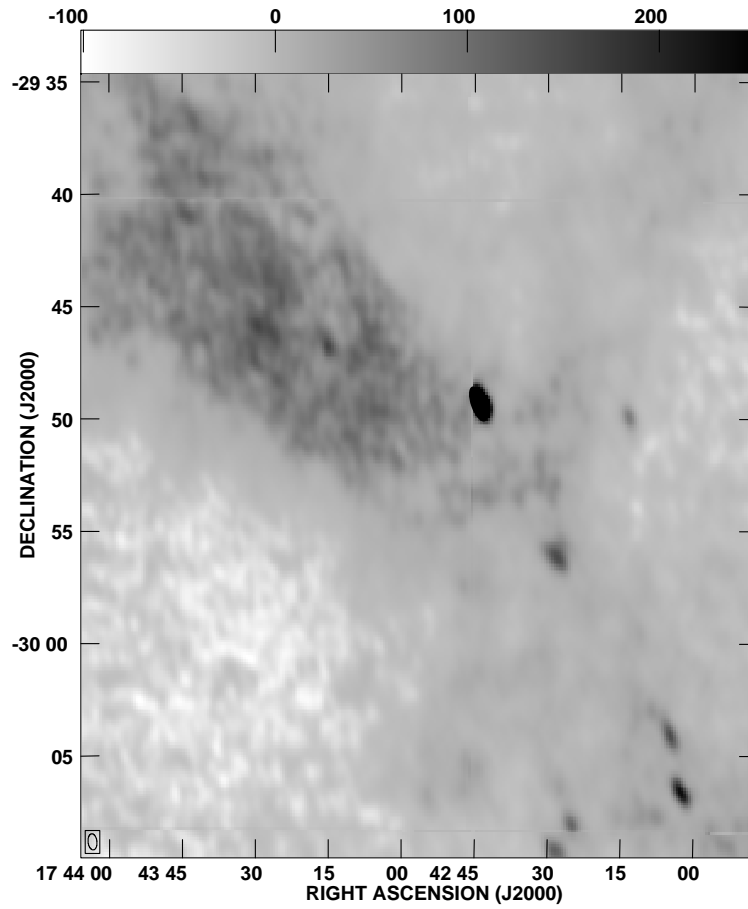


FIG. 3b

FIG. 3.—Wide-field imaging of a point source: two-dimensional vs. three-dimensional. (a) Distorted response to a point source located far ($>1^\circ$) from the field center from the original two-dimensional processed 330 MHz image. (b) Undistorted subimage of Fig. 1 made to the same scale and of approximately the same region as shown to the left. The three-dimensional image reveals many more sources, possibly including an extended emission feature labeled “Coherent structure?” on Fig. 1.

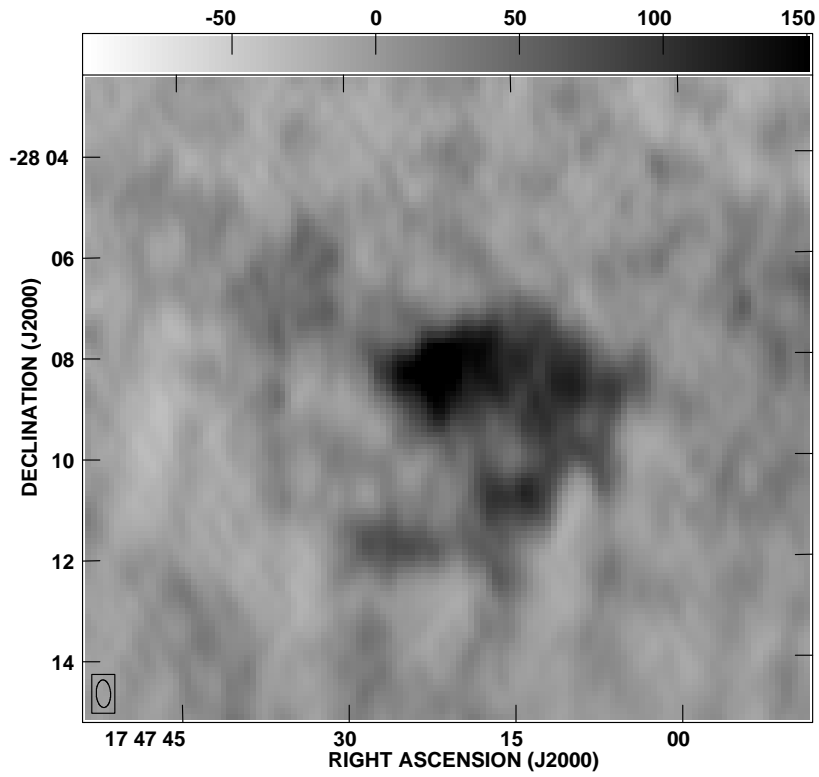


FIG. 4a

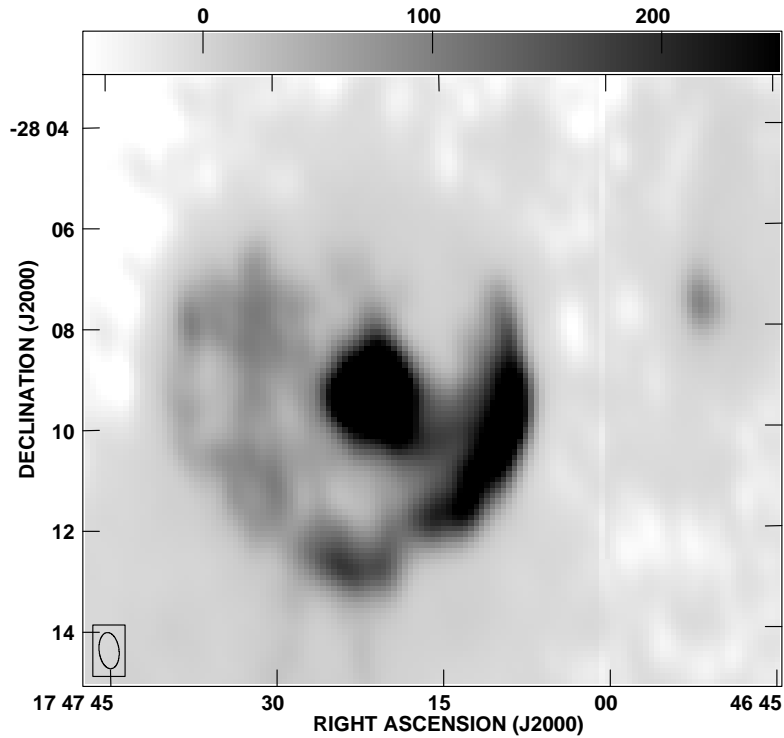


FIG. 4b

FIG. 4.—Wide-field imaging of an extended source: two-dimensional vs. three-dimensional. (a) Distorted response to SNR $0.9 + 0.1$ located far ($> 1^\circ$) from the field center from the original two-dimensional processed 330 MHz image. (b) Subimage of Fig. 1 made to the same scale and of approximately the same region. The undistorted image reveals the accurate shell and plerionic emission of this composite SNR.

assumption of a coplanar array and a two-dimensional inversion is justified. This polyhedral algorithm has been implemented by Kassim, Briggs, & Foster (1998) and ported to supercomputing platforms available through the Depart-

ment of Defense High-Performance Computing Modernization Program. This program, Dragon, is now utilized routinely to generate both 74 and 330 MHz VLA images with sensitivities near the thermal- or classical-confusion

noise limits. Figures 3 and 4 show the dramatic improvement in image fidelity for both point and extended sources located far from the phase center of the image, when the proper three-dimensional imaging is performed. The increase in image fidelity and the concomitant reduction in the noise level in Figure 1 has allowed us to identify a number of sources that could not be detected in the original two-dimensional image. The new three-dimensional processed image covers $4^\circ \times 5^\circ$ with a resolution of $43'' \times 24''$ and a rms sensitivity of 5 mJy beam^{-1} (away from the strong emission on the Galactic ridge). The largest angular scale to which this image is sensitive is approximately $45'$.

3. CATALOG OF SOURCES

The improved sensitivity and image quality of the three-dimensional image processing has resulted in a map with an extraordinarily large number of distinct sources. In order to facilitate comparison with other wavelength observations and to establish a baseline epoch of observations, we have cataloged over a hundred sources from the new image. The catalog consists of 23 extended sources and 78 small-diameter sources and is presented in Tables 1 and 2, respectively.

3.1. Extended Sources

In Table 1, column (1) lists the names of the sources we have identified. The names are either conventional (e.g., Sgr A) or are derived from Galactic coordinates. For newly

identified sources, we have assigned their names based on the location of peak brightness. Columns (2), (3), (4), and (5) report the Galactic and equatorial (J2000.0) coordinates, respectively, of the sources. Column (6) reports the approximate diameters of the sources in arcminutes. Columns (7) and (8) report the peak intensities in Jy beam^{-1} and the integrated flux densities in Jy, respectively. Column (9) contains comments on individual sources.

Flux densities for these sources were determined in the following manner. First, the brightness distribution was integrated over a polyhedral region enclosing each source. In order to determine the background level, the brightness distribution within an annular region surrounding each source was also integrated. The flux density of the source was taken to be the difference between the integrations over the polyhedral and annular regions, where the latter was normalized by the ratio of the areas of the two regions. Because many of these sources do not have sharply defined boundaries, the above procedure was repeated five times, with slightly different polyhedral and annular regions. The reported flux densities and uncertainties are the mean and standard deviation of the five trials. The five trials were also used to establish a mean background brightness. The reported peak intensity for a source has had this mean background level subtracted. Of course, the flux densities and intensities we report, strictly speaking, should be taken as lower limits, because we are not sensitive to structures on scales larger than approximately $45'$. In this respect, the flux

TABLE 1
GALACTIC CENTER 330 MHz SOURCE LIST: EXTENDED SOURCES

Source (1)	l (2)	b (3)	R.A. (4)	Decl. (5)	Size (arcmin) (6)	I (Jy beam^{-1}) (7)	S_{90} (Jy) (8)	Remarks (9)
Tornado	357.65	-0.08	17 40 14	-30 58 43	7.4×5.1	... ^a	... ^a	SNR
G359.0-0.9	359.03	-0.96	17 47 30	-30 08 59	Irregular	0.23	105.16 ± 5.00	SNR
G359.07-0.02	359.07	-0.02	17 43 29	-29 45 55	22×10	0.16	38.59 ± 1.33	Possible SNR
G359.10-0.5	359.10	-0.51	17 44 59	-29 51 11	21×21	0.17	71.95 ± 3.00	SNR
G359.15-0.2	359.15	-0.17	17 44 20	-29 46 27	5.2×0.9	0.10	0.61 ± 0.11	The Snake
Mouse	359.30	-0.82	17 47 11	-29 57 59	2.6×1.8	0.43	1.43 ± 0.01	Foreground object
G359.43-0.09	359.43	-0.09	17 44 36	-29 28 03	1.3×0.6	0.18	0.72 ± 0.02	H II Region $\alpha^{90/20} = 0.13 \pm 0.03$
Sgr C	359.45	-0.01	17 44 28	-29 25 19	11.1×0.7	0.51	6.39 ± 0.81	Nonthermal filament (NTF)
G359.54+0.18	359.55	0.17	17 43 54	-29 13 51	6.1×1.1	0.19	1.48 ± 0.40	NTF
G359.79+0.17	359.80	0.16	17 44 29	-29 01 35	6.5×1.4	0.3	2.22 ± 0.09	NTF
G359.85+0.47	358.85	0.47	17 41 00	-29 39 53	4.6×0.9	0.12	0.70 ± 0.10	NTF the Pelican
G359.87+0.44	359.87	0.44	17 43 44	-28 51 19	Irregular	0.04	1.30 ± 0.22	New source the Cane
G359.91-1.03	359.91	-1.03	17 49 28	-29 32 07	2.3×0.6	0.12	0.66 ± 0.02	Possible NTF
Sgr A	359.95	-0.05	17 45 44	-28 59 15	13.5×13.5	8.32	361.50 ± 14.85	Center region
G359.96+0.09	359.96	0.11	17 45 15	-28 55 36	11.6×0.7	0.15	1.18 ± 0.07	NTF southern thread
G0.09+0.17	0.09	0.17	17 45 13	-28 46 50	11.9×0.8	0.28	3.49 ± 0.09	NTF northern thread
GCRA	0.18	-0.07	17 46 35	-28 52 28	28.5×4.0	0.54	38.50 ± 7.78	The radio arc
G0.30+0.04	0.31	0.04	17 46 09	-28 42 59	12.1×7.8	0.24	35.95 ± 2.66	SNR
Sgr B1	0.52	-0.05	17 47 01	-28 30 59	7.0×6.5	0.22	14.01 ± 0.69	H II region complex
Sgr B2	0.64	-0.06	17 47 20	-28 23 09	7.3×7.2	0.47	17.42 ± 0.81	H II region complex
SNR 0.9+0.1	0.86	0.07	17 47 21	-28 09 23	7.2×7.0	0.53	16.12 ± 0.73	Composite SNR
SNR 0.9+0.1	0.87	0.08	17 47 23	-28 09 21	1.7×1.3	0.52	4.80 ± 0.07	Core of composite SNR
Sgr D	1.02	-0.17	17 48 36	-28 05 45	9.8×8.0	0.32	23.41 ± 0.93	Sgr D SNR
Sgr D	1.12	-0.07	17 48 42	-28 01 30	7.5×6.4	0.31	17.75 ± 0.76	Sgr D H II Region

NOTE.—Units of right ascension are hours, minutes, and seconds, and units of declination are degrees, arcminutes, and arcseconds (J2000.0).

^a The peak and integrated flux densities of the Tornado were not estimated because of severe primary beam attenuation at its location near the edge of the field of view.

TABLE 2
GALACTIC CENTER 330 MHz SOURCE LIST: SMALL-DIAMETER SOURCES

Source Number (1)	Name (2)	R.A. (3)	Decl. (4)	θ (arcmin) (5)	I (Jy beam ⁻¹) (6)	S_{90} (Jy) (7)	S_{20}^a (Jy) (8)	$\alpha^{90/20}$ (9)	Offset (arcmin) (10)	ID (11)	Survey/Name (12)
1.....	358.15+0.03	17 41 03	-30 29 35	0.5	0.17	0.37 ± 0.02	0.056 ± 0.002	-1.31 ± 0.05	111.6		LS95, GPSR
2.....	358.59+0.05	17 42 03	-30 06 37	0.3	0.23	0.42 ± 0.03	0.046 ± 0.002	-1.54 ± 0.06	85.3	xgal	Sgr E 18, GPSR
3.....	358.61-0.06	17 42 29	-30 09 13	0.6	0.12	0.30 ± 0.07	0.559 ± 0.019	0.43 ± 0.16	84.3	H II region	Sgr E 33, GPSR
4.....	358.61-0.03	17 42 25	-30 08 03	0.2	0.10	0.16 ± 0.01			83.3	xgal	Sgr E 29
5.....	358.63+0.06	17 42 05	-30 04 05	0.3	0.13	0.30 ± 0.02	0.367 ± 0.013	0.14 ± 0.05	83.0	H II region	Sgr E 19, GPSR
6.....	358.69-0.08	17 42 47	-30 05 47	1.5	0.03	0.27 ± 0.02	0.035 ± 0.001 ^e	-1.42 ± 0.06	79.3		PM75
7.....	358.69-0.11	17 42 55	-30 06 39	1.4	0.03	0.21 ± 0.07	0.123 ± 0.004	-0.37 ± 0.23	79.3		GPSR
8.....	358.79+0.06	17 42 28	-29 56 04	0.9	0.14	0.50 ± 0.02	0.360 ± 0.013	-0.23 ± 0.04	73.7	H II region	Sgr E 30
9.....	358.85+0.16	17 42 14	-29 49 56	0.4	0.08	0.15 ± 0.01	0.035 ± 0.001	-1.01 ± 0.05	70.9	xgal	Sgr E 23, GPSR
10.....	358.92+0.07	17 42 44	-29 49 18	0.3	1.39	2.14 ± 0.01	0.402 ± 0.014	-1.16 ± 0.02	66.1	xgal	Sgr E 46, GPSR
11.....	358.94-1.21	17 47 50	-30 28 11	0.6	0.20	0.48 ± 0.01	0.059 ± 0.002	-1.46 ± 0.03	93.1		TXS 1744-304
12.....	358.98+0.58	17 40 55	-29 29 46	0.5	0.10	0.21 ± 0.01	0.070 ± 0.002	-0.77 ± 0.04	73.5		
13.....	359.16+0.96	17 39 51	-29 08 39	0.5	0.07	0.09 ± 0.01	0.003 ± 0.001	-2.37 ± 0.24	81.0		LS95
14.....	359.28-0.26	17 44 55	-29 41 06	0.6	0.07	0.15 ± 0.01	0.773 ± 0.023 ^e	1.14 ± 0.05	45.3		LS95 ^d , GPSR
15.....	359.30-0.13	17 44 28	-29 36 10	0.3	0.09	0.13 ± 0.01			42.9		LS95
16.....	359.33-0.15	17 44 37	-29 35 35	0.5	0.12	0.27 ± 0.03			41.4		
17.....	359.33+0.48	17 42 08	-29 15 25	0.7	0.02	0.06 ± 0.01			53.2		
18.....	359.35+0.52	17 42 02	-29 13 07	0.6	0.03	0.05 ± 0.01	0.033 ± 0.003	-0.29 ± 0.15	53.8		
19.....	359.36+0.49	17 42 12	-29 13 30	0.5	0.04	0.08 ± 0.01			51.8		
20.....	359.37+0.10	17 43 43	-29 25 18	0.2	0.03	0.07 ± 0.00	0.054 ± 0.002	-0.18 ± 0.04	40.1		
21.....	359.39-0.07	17 44 27	-29 29 36	0.7	0.20	0.72 ± 0.10	0.129 ± 0.005	-1.20 ± 0.10	37.3		LS95, GPSR
22.....	359.39+0.46	17 42 21	-29 12 58	0.5	0.08	0.16 ± 0.01	0.036 ± 0.001	-1.04 ± 0.05	49.5		TXS 1736-287
23.....	359.39+1.27	17 39 13	-28 46 59	0.5	0.16	0.40 ± 0.04	0.132 ± 0.005	-0.77 ± 0.07	89.2		
24.....	359.43+0.13	17 43 45	-29 21 20	0.7	0.09	0.31 ± 0.01			37.2		
25.....	359.47+1.25	17 39 31	-28 43 31	0.6	0.11	0.31 ± 0.02	0.049 ± 0.002	-1.28 ± 0.05	85.8		LS95
26.....	359.47-0.17	17 45 01	-29 28 36	0.7	0.07	0.20 ± 0.03			33.1		
27.....	359.50-0.31	17 45 39	-29 31 42	0.9	0.03	0.14 ± 0.03			33.9		
28.....	359.50+0.39	17 42 55	-29 09 14	0.7	0.03	0.08 ± 0.01			41.6		
29.....	359.52+0.14	17 43 56	-29 16 35	0.8	0.06	0.11 ± 0.02			32.5		
30.....	359.55+0.99	17 40 42	-28 48 08	0.4	0.11	0.21 ± 0.01			69.8		TXS 1737-287
31.....	359.56+0.80	17 41 26	-28 53 34	0.4	0.03	0.05 ± 0.01	0.073 ± 0.003	-0.74 ± 0.04	59.6		
32.....	359.57+1.15	17 40 08	-28 42 02	0.5	0.16	0.36 ± 0.01	0.029 ± 0.002	-0.38 ± 0.15	78.2		
33.....	359.59+0.03	17 44 32	-29 16 33	0.5	0.03	0.05 ± 0.00	0.225 ± 0.008	-0.33 ± 0.03	26.4		
34.....	359.60+0.31	17 43 29	-29 06 47	0.3	0.13	0.18 ± 0.01			33.7		GPSR
35.....	359.63+1.31	17 39 38	-28 33 46	0.6	0.12	0.35 ± 0.03	0.083 ± 0.003	-1.00 ± 0.06	87.3		
36.....	359.65-0.08	17 45 05	-29 16 45	1.1	0.15	0.77 ± 0.05	... ^b		21.9		LS95
37.....	359.65-0.06	17 44 59	-29 16 03	0.4	0.06	0.12 ± 0.02	... ^b		22.0		LS95
38.....	359.70+0.31	17 43 42	-29 01 43	0.5	0.04	0.08 ± 0.00	... ^b		30.1		
39.....	359.71-0.90	17 48 29	-29 39 09	0.3	0.22	0.35 ± 0.02	0.050 ± 0.002	-1.36 ± 0.05	52.7		LS95, PM75
40.....	359.73-0.04	17 45 06	-29 11 18	0.9	0.15	0.66 ± 0.15	... ^b		17.5		
41.....	359.77-0.28	17 46 10	-29 16 28	0.5	0.09	0.17 ± 0.01	... ^b		18.6		
42.....	359.78+0.53	17 43 03	-28 51 01	0.3	0.04	0.06 ± 0.01			38.9		
43.....	359.85-1.85	17 52 31	-30 01 08	0.6	0.29	0.76 ± 0.03	0.351 ± 0.011	-0.54 ± 0.04	105.9		
44.....	359.87+0.18	17 44 37	-28 57 08	0.3	0.31	0.44 ± 0.01	... ^b		17.8		YCR98, GPSR
45.....	359.91-1.81	17 52 33	-29 56 35	0.8	0.16	0.62 ± 0.05	0.235 ± 0.008	-0.68 ± 0.06	103.5		
46.....	359.99+1.59	17 39 27	-28 06 13	0.4	0.09	0.15 ± 0.01	0.074 ± 0.002	-0.49 ± 0.05	100.7		

TABLE 2—Continued

Source Number (1)	Name (2)	R.A. (3)	Decl. (4)	θ (arcmin) (5)	I (Jy beam ⁻¹) (6)	S_{90} (Jy) (7)	S_{20}^a (Jy) (8)	$\alpha^{90/20}$ (9)	Offset (arcmin) (10)	ID (11)	Survey/Name (12)
47	0.00−0.89	17 49 07	−29 23 45	0.5	0.37	0.70 ± 0.02	0.214 ± 0.007	−0.83 ± 0.03	48.7		
48	0.05+0.51	17 43 45	−28 37 23	0.7	0.03	0.09 ± 0.01			35.9		TG91
49	0.07−0.68	17 48 28	−29 13 44	0.5	0.05	0.12 ± 0.01	0.022 ± 0.002	−1.18 ± 0.09	36.6		
50	0.17−0.53	17 48 05	−29 04 01	0.5	0.03	0.08 ± 0.00	...		28.3		
51	0.22−0.50	17 48 05	−29 00 28	0.3	0.03	0.05 ± 0.00	...		27.7		
52	0.27+1.20	17 41 38	−28 04 34	0.5	0.14	0.29 ± 0.01	0.045 ± 0.001	−1.30 ± 0.03	78.5		
53	0.31+1.65	17 40 01	−27 48 06	0.8	0.10	0.32 ± 0.08	0.170 ± 0.006	−0.44 ± 0.18	105.8		
54	0.38+0.02	17 46 28	−28 36 02	0.8	0.15	0.55 ± 0.05	...		23.0	SNR	KF96, GPSR
55	0.40+1.06	17 42 28	−28 02 13	0.3	0.19	0.32 ± 0.02	0.063 ± 0.002	−1.13 ± 0.05	72.7		
56	0.41+0.98	17 42 47	−28 04 29	0.5	0.05	0.08 ± 0.01	0.036 ± 0.002	−0.56 ± 0.10	68.0		
57	0.44+0.59	17 44 23	−28 14 58	0.5	0.14	0.25 ± 0.01			47.9		
58	0.47−0.64	17 49 13	−28 51 55	0.6	0.05	0.11 ± 0.00			43.0		
59	0.58−0.87	17 50 24	−28 53 15	0.7	0.11	0.36 ± 0.01	0.574 ± 0.021	0.32 ± 0.03	53.6		PM75
60	0.60−0.05	17 47 14	−28 26 51	0.4	0.08	0.17 ± 0.02	...		35.4	Sgr B2	MPG95
61	0.63−0.03	17 47 13	−28 24 47	0.8	0.17	0.53 ± 0.07	...		37.2	Sgr B2	MPG95, PM75
62	0.64−0.06	17 47 22	−28 25 17	0.9	0.14	0.66 ± 0.06	...		37.6	Sgr B2	MPG95
63	0.64−0.11	17 47 34	−28 26 51	1.2	0.19	1.23 ± 0.23	...		37.6	Sgr B2	
64	0.66+1.06	17 43 06	−27 49 26	0.4	0.12	0.21 ± 0.01	0.077 ± 0.002	−0.70 ± 0.04	78.6		
65	0.66−0.01	17 47 13	−28 22 55	1.1	0.18	0.85 ± 0.15	...		38.8	Sgr B2	MPG95, PM75
66	0.67−0.04	17 47 20	−28 23 11	0.8	0.33	1.11 ± 0.07	...		39.3	Sgr B2	MPG95
67	0.73−0.10	17 47 44	−28 21 48	1.1	0.20	1.07 ± 0.03	...		43.2		PM75, GPSR
68	0.83−0.11	17 48 01	−28 16 22	0.6	0.04	0.16 ± 0.01	...		49.8		
69	0.84+0.19	17 46 52	−28 07 32	0.6	0.09	0.21 ± 0.01	...		52.1		GPSR
70	0.85+1.17	17 43 06	−27 36 03	0.4	0.28	0.51 ± 0.01	0.160 ± 0.005	−0.81 ± 0.03	87.9		
71	0.87−0.28	17 48 47	−28 20 07	0.4	0.04	0.07 ± 0.01	...		53.2		GPSR
72	1.03−1.11	17 52 23	−28 37 40	0.7	0.32	1.00 ± 0.03	0.244 ± 0.007	−0.98 ± 0.03	87.4		
73	1.03+1.55	17 42 05	−27 15 00	0.4	0.24	0.61 ± 0.06	0.050 ± 0.002	−1.74 ± 0.07	115.4		
74	1.05+1.57	17 42 02	−27 13 17	0.5	0.47	1.04 ± 0.08	0.205 ± 0.008	−1.13 ± 0.06	117.3		
75	1.42+0.26	17 47 58	−27 35 12	0.2	0.04	0.04 ± 0.01			87.4		
76	1.47+0.24	17 48 09	−27 33 44	0.5	0.15	0.35 ± 0.01	0.060 ± 0.002	−1.23 ± 0.03	89.2		GPSR, TXS 1745−275
77	1.54−0.96	17 52 59	−28 06 36	0.6	0.44	1.28 ± 0.03	0.042 ± 0.001	−2.38 ± 0.02	106.2	psr	PSR B1749−28
78	1.88+0.33	17 48 46	−27 09 48	1.1	0.57	2.84 ± 0.10	0.747 ± 0.250	−0.93 ± 0.23	114.5	SNR	GPSR, TXS 1745−271

NOTES.—Units of right ascension are hours, minutes, and seconds, and units of declination are degrees, arcminutes, and arcseconds (J2000.0). Identifications are SNR, supernova remnant; psr, radio pulsar; Sgr B2, presumed H II region; xgal, extragalactic source.

^a 20 cm flux densities obtained from the NVSS.

^b Source position is within central confused region of NVSS image.

^c Source corresponds to two NVSS sources. S_{20} is the sum of both NVSS counterparts.

^d Source not catalogued in LS95 but is visible on their 20 cm image with $S_{20} = 25.6$ mJy.

REFERENCES.—(GPSR) Zoonematkermani et al. (1990) and/or Becker et al. (1994); (KF96) Kassim & Frail (1996); (LS95) Liszt & Spiker (1995); (MPG95) Mehringer et al. (1995); (PM75) Pauls & Mezger (1975); (TG91) Terzan & Gosset (1991); (YCR98) Yusef-Zadeh et al. (1997); (TXS) Douglas et al. (1996).

density of Sgr A in particular should be considered a rough estimate since it is quite difficult to distinguish between the different components and the background at this resolution.

3.2. Small-Diameter Sources

Small-diameter sources were initially selected visually. The local background level and rms noise level was then determined for each source. Only sources with peak intensity to background ratios greater than 5σ are included in Table 2. Figure 5 indicates the positions of these small-diameter sources, and column (1) of Table 2 lists the source numbers. Columns (2), (3), and (4) report the source positions in Galactic and equatorial coordinates (J2000.0), respectively. Column (5) reports the geometric means of the (deconvolved) major and minor axes, in arcminutes. Columns (6) and (7) report the peak intensities and integrated flux densities in Jy beam^{-1} and Jy, respectively.

The position, peak intensity, integrated flux density, and beam-deconvolved size for a source were determined using the AIPS task IMFIT, which fits a Gaussian and background level to a source within a specified region. Similar to our procedure for extended sources, IMFIT was run five different times with slightly different fitting regions, for each source. We report the mean and standard deviation from these five trials.

Column (8) lists the flux densities of counterparts to our small-diameter sources found in the 1400 MHz NVSS catalogue (Condon et al. 1998). (We note that this single snapshot survey has limited $[u, v]$ coverage for extended sources.) The resolution of the NVSS survey is $45'' \times 45''$,

similar to our 90 cm resolution of $43'' \times 24''$. The NVSS sources listed are all within one beam of our source positions. As a consistency check of our source measuring technique, we obtained NVSS maps of our field of view and measured approximately 20 sources, using the same procedure that we employed for the sources that we identified at 90 cm. Our estimates for source parameters were in agreement with those listed in the NVSS catalogue. For each source with an NVSS counterpart, the spectral index was derived and is listed in column (9). Nineteen of our small-diameter sources are within the central portion of the field, a highly confused area for the NVSS. Although there are nominal NVSS counterparts to eight of these sources, we have not attempted to estimate their spectral indices.

We have corrected our flux density estimates for the primary beam attenuation. Because this attenuation, as well as bandwidth smearing (see below), depend upon the distance from the center of the image, column (10) reports the offset of each source from the phase center of the image.

Sources in the outer portions of the map (e.g., those in Sgr E) appear elongated toward the center as a result of bandwidth smearing. Because our beam is asymmetric, the extent of bandwidth smearing depends on both the offset and orientation of a source with respect to the center of the map. The ratio of the peak to integrated intensities versus source size shows a strong correlation, with greater ratios corresponding to smaller sizes, as would be expected for bandwidth-smear, unresolved sources.

In order to verify that this is indeed the case, we convolved our image to a symmetrical resolution of $45'' \times 45''$

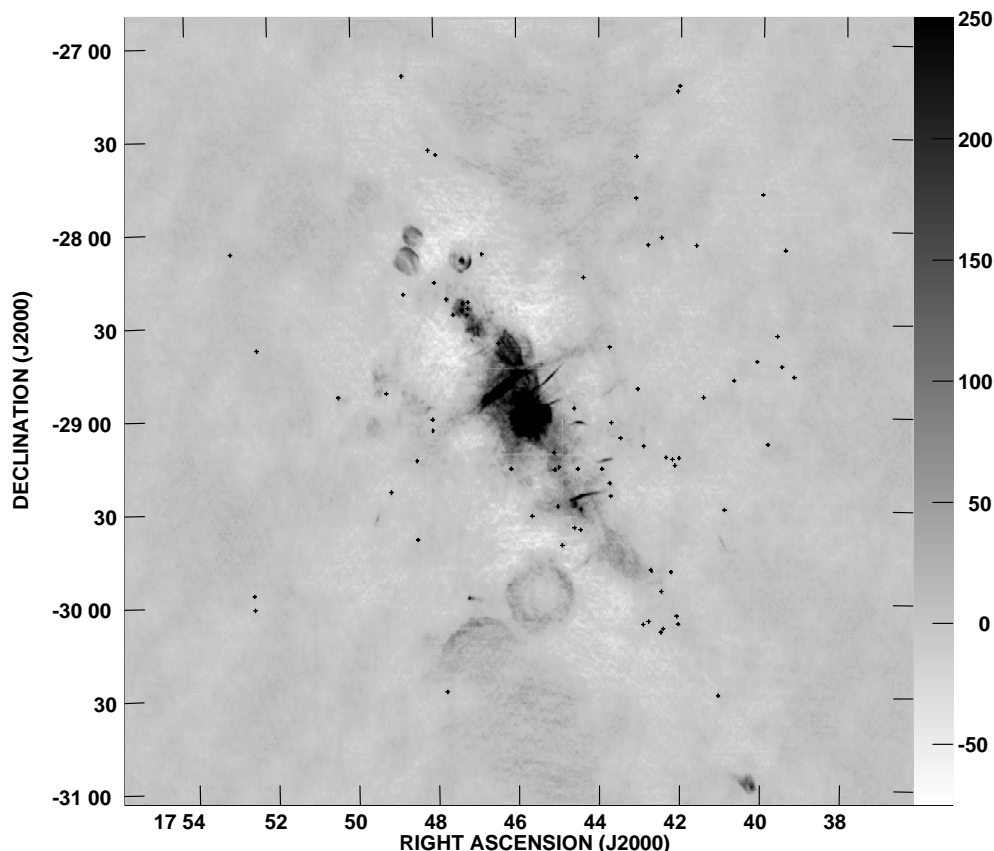


FIG. 5.—Locations of small-diameter sources listed in Table 2. This image shows the full $4^\circ \times 5^\circ$ field. The image has not been corrected for primary beam attenuation. The gray-scale levels in mJy beam^{-1} are useful for estimating relative flux densities only.

and examined well-isolated sources approximately 1° – 2° from the phase center. The peak intensity reduction and the elongation of these sources on the convolved image are consistent with those predicted using the algorithm in Bridle & Schwab (1988). As only a small number of our sources are relatively close to the phase center of the map, most of the deconvolved sizes and peak intensities listed in Table 2 are affected by bandwidth smearing. In addition, because IMFIT cannot fit the background perfectly, the fitted size will be larger than a beam for many point sources. Despite these limitations, we have still included the sizes and peak intensities in Table 2 because we cannot categorically rule out the possibility that some are resolved.

Finally, in column (11) we indicate counterparts found within one beam of various surveys toward the GC. We note that including results from our NVSS search and a search of the SIMBAD databases, we find references to all of the sources in Table 2 except 17, 24, 28, 42, 50, and 51. The brightest of these is source 24, which has an integrated flux density of 310 mJy, while the others are all below 100 mJy. We have also searched the ROSAT X-ray source database and find no counterparts to these sources.

4. DESCRIPTION OF INDIVIDUAL EXTENDED SOURCES

In this section we present images and brief discussions of most of the extended sources. We will not discuss Sgr A or the Radio Arc because Pedlar et al. (1989) and Anantharamaiah et al. (1991) have already discussed them in some detail.

However, for completeness we present both gray-scale and contour plots for Sgr A and its surroundings. Figure 6 shows Sgr A East and its halo and the region around Sgr A including the GCRA.

For many of the sources we measure their spectral indices. We estimate that typical uncertainties in the spectral index measurements are ± 0.1 .

4.1. *G0.33+0.00*

This source was first recognized in an 80 MHz Clark Lake image of the GC region (LaRosa & Kassim 1985). Recently Kassim & Frail (1996), based on the original Pedlar et al. (1989) data and 20 cm archival VLA, concluded that *G0.33+0.00* is an SNR. We confirm their integrated 90 cm flux and present slightly improved images. Figure 7 indicates that *G0.33+0.00* may be superposed on another shell of nonthermal emission. This partial shell lies just outside the western boundary of *G0.33+0.00* and has a surface brightness about a factor of 2 to 3 lower than *G0.33+0.00*. We speculate that this source is a supernova remnant (SNR).

4.2. *G0.9+0.1*

Figure 8 shows this supernova remnant to have two components. Earlier observations of these two components led Helfand & Becker (1987) to classify this SNR as a composite based on radio observations of a flat spectrum core component ($\approx 2'$ in diameter) and a steep spectrum shell component with a radius of about $7.5'$. Recently, Mereghetti, Sidoli, & Israel (1998) detected X-ray emission from the core component of *G0.9+0.1* with the BeppoSAX satellite. They were able to fit the X-ray spectrum with a power law and interpret the X-ray emission as nonthermal in origin. The small angular extent of the X-ray emission, combined with an estimated age of the remnant of a few thousand

years, is further evidence that the core is powered by a young pulsar. Our flux density measurements of the shell (≈ 16 Jy) and core (≈ 3.5 Jy), combined with 20 cm VLA measurements of Liszt (1992), yield spectral indices (α) of the shell of -0.77 and core of 0.12 . These are consistent with previous estimates of the spectral indices and confirm the composite classification of this SNR.

4.3. *G1.05-0.1 (Sgr D SNR)*

This source has a filled-shell morphology and is identified as a shell-type SNR in A Catalogue of Galactic Supernovae Remnants by D. A. Green.² In contrast to our image (Fig. 9), which shows that this source has a well-defined boundary around the entire circumference, 20 cm observations (Liszt 1992) show a bright northern rim and a very diffuse southern boundary. At 6 cm only the northern rim of this source is detected (Mehring et al. 1998). Previous observations reported by Green indicate a nonthermal spectral index of -0.6 .² Combining our flux density measurement with those in the literature (375 cm, LaRosa & Kassim 1985; 74 cm, Little 1974; 36 cm, Gray 1994a; 18 cm, Liszt 1992; and 6 cm, Mehringer et al. 1998) yields a spectral index of -0.4 .

4.4. *G359.0-0.9*

Figure 10 shows this source to be a partial shell with a very bright northern rim. It is not known if this source is a GC or local object. Unfortunately, at 90 cm this source is located in a region of fairly high noise, which prevented an unambiguous background subtraction. We decided to integrate the flux only over regions where the signal-to-noise ratio was above 5σ even though the source appeared to extend well beyond this limit. Our flux density estimate should therefore be considered as a lower limit. Using this lower limit of 40 Jy with the higher frequency observations of Reich, Sofue, & Fürst (1987), we obtain a spectral index of -0.5 , consistent with their estimates. As our flux density is a lower limit the actual spectrum is likely to be steeper.

4.5. *G359.1-0.5*

Figure 11 shows this source to be a large, symmetric shell. Reich & Fürst (1984) classified it as a SNR on the basis of its nonthermal spectrum ($\alpha = -0.37$) and polarized emission. H I absorption-line observations suggest that this object is located at the Galactic center and possibly associated with the nonthermal filament known as the Snake (Uchida, Morris, & Yusef-Zadeh 1992b; § 4.8.6). This shell is also surrounded by a ring of high velocity molecular gas. The mass of this ring and its energetics imply that the shell may in fact be a superbubble driven by a cluster of roughly 200 O stars (Uchida et al. 1992b).

At 90 cm this source is situated in region with a considerable negative background. Given the shell's large size and the uncertain background, we did not attempt a background subtraction. Consequently our flux density estimate should be considered a lower limit. Using the flux densities measured at shorter wavelengths (6 and 11 cm, Reich & Fürst 1984) with our 90 cm flux of 43 Jy yields a spectral index of -0.7 , considerably steeper than the index determined using only the high-frequency observations. Once

² Made available by the Mullard Radio Astronomy Observatory, Cambridge, United Kingdom, at <http://www.mrao.cam.ac.uk/surveys/snr/>.

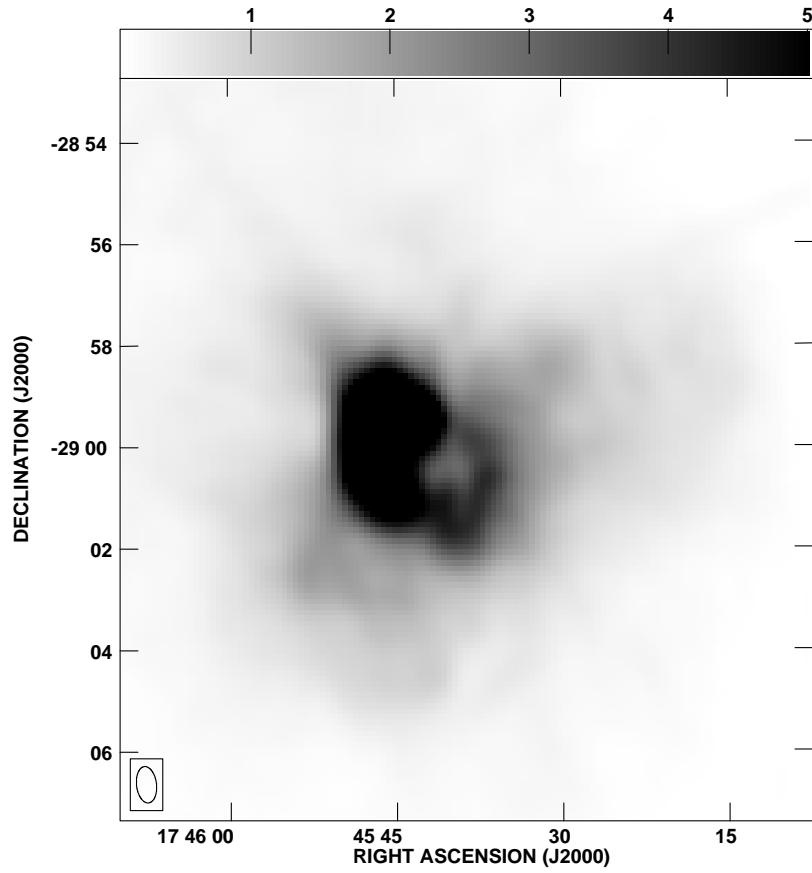


FIG. 6a

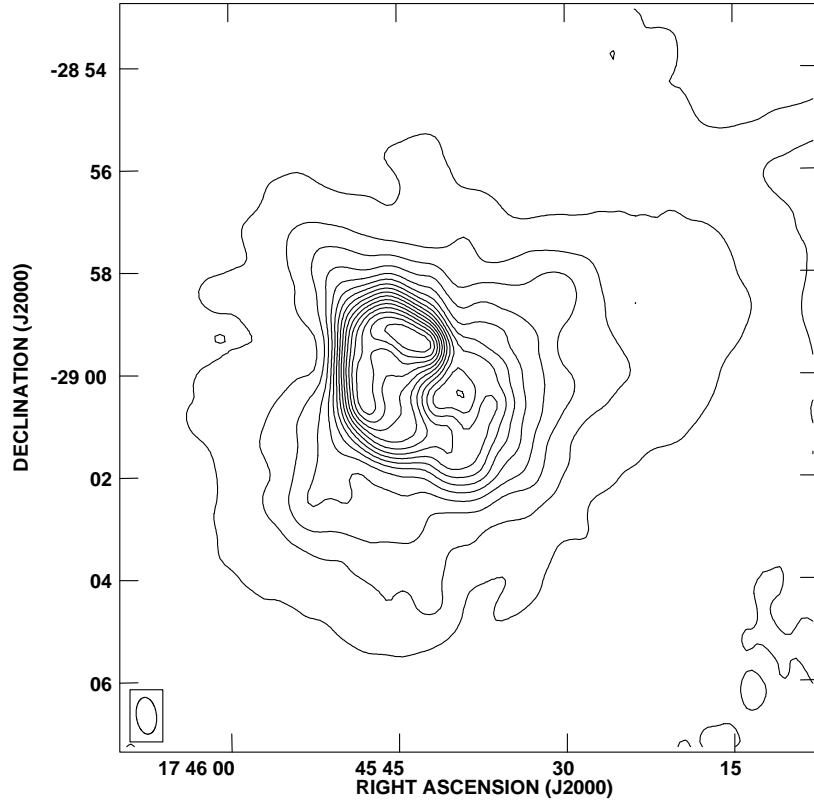


FIG. 6b

FIG. 6.—Images of Sgr A and surroundings. (a) Gray scale of Sgr A East and its halo; levels are linear and in units of Jy beam^{-1} . (b) Contour map of Sgr A East and its halo; levels are 0.5, 1, 1.5, 2, 3, 4, 5, 6, 7, and 8 Jy beam^{-1} . (c) Gray scale of Sgr A and the GCRA, levels are linear and in units of Jy beam^{-1} . (d) Contour of Sgr A and the GCRA; levels are $-0.01, 0.1, 0.2, 0.3, 0.4, 0.5, 0.6, 0.7, 0.8, 0.9$, and 1 Jy beam^{-1} . The beam is shown in the lower left.

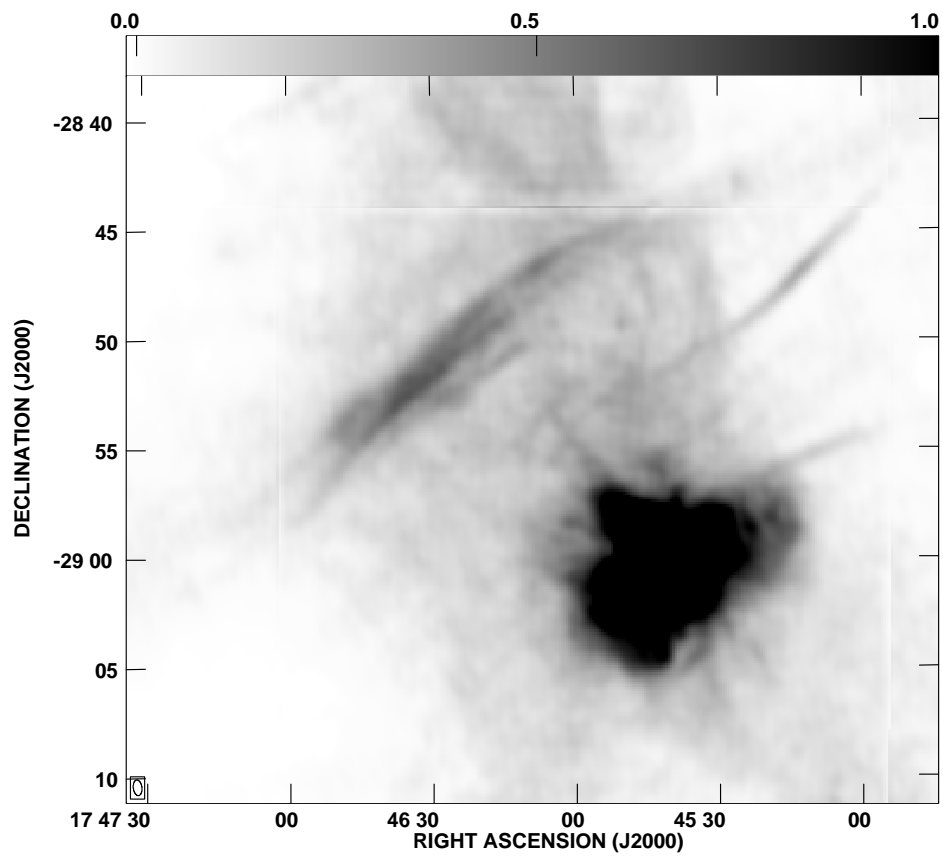


FIG. 6c

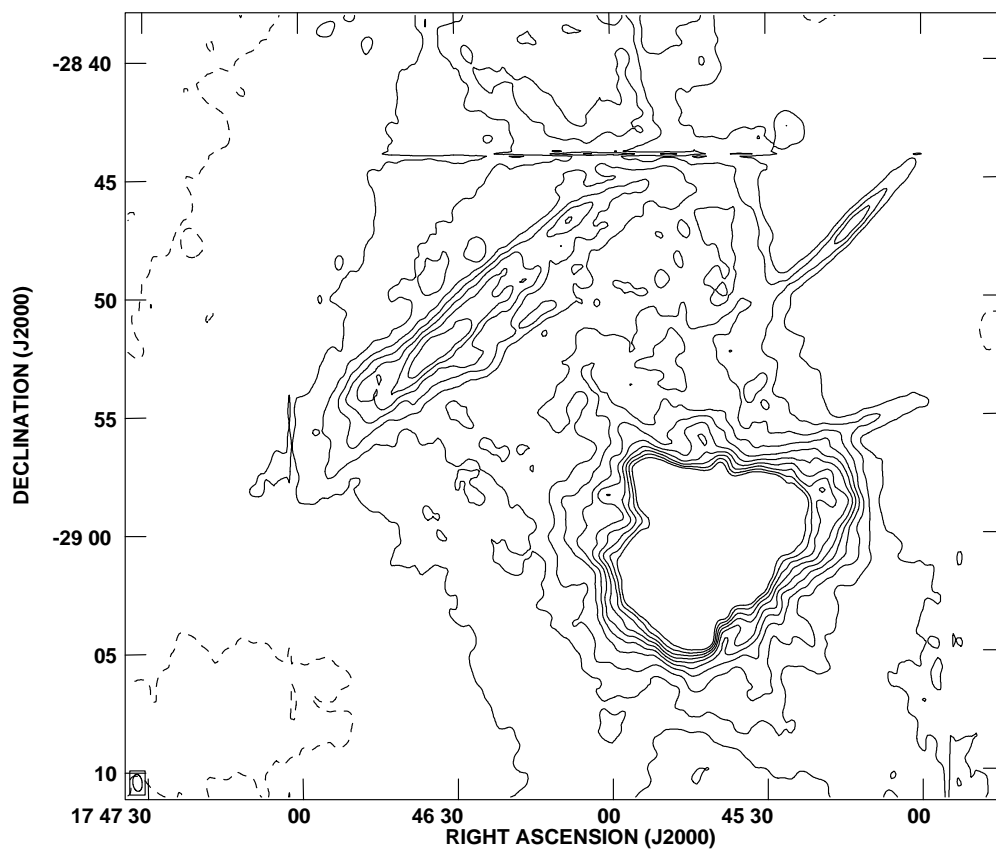


FIG. 6d

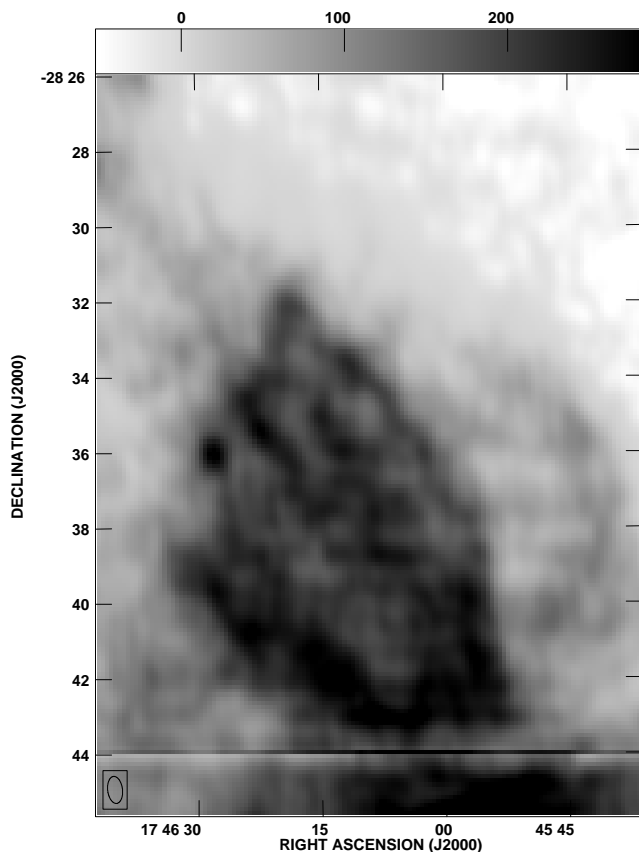


FIG. 7a

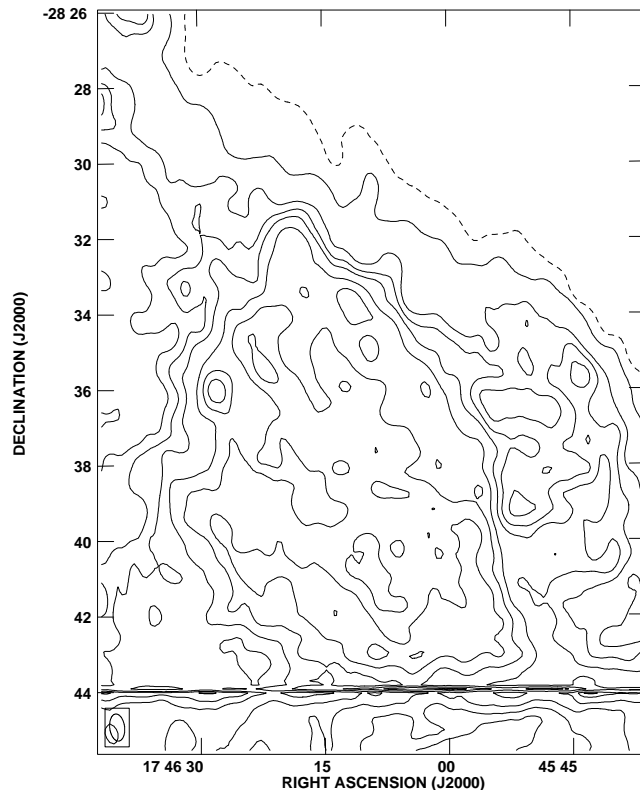


FIG. 7b

FIG. 7.—Images of G0.33+0.00. (a) Gray-scale levels are linear and in units of mJy beam^{-1} . (b) Contour levels are $-5, 1, 10, 25, 50, 75, 100, 150, 200, 250$, and $300 \text{ mJy beam}^{-1}$. The beam is shown in the lower left.

again, as our flux density is a lower limit, the actual spectrum may be even steeper.

4.6. G359.3−0.82 (*The Mouse*)

This cometary radio source is known to be a foreground object and is not associated with G359.1−0.5 or G359.0−0.9 (Uchida et al. 1992b). This emission from the tail of the source is polarized and has a spectral index between -0.1 to -0.3 (Yusef-Zadeh & Bally 1989).

Figure 12 shows that the “Mouse” is clearly resolved at 90 cm. Using the NVSS 20 cm flux we estimate the spectral index between 20 and 90 cm to be -0.43 ± 0.1 .

4.7. G357.7−0.1 (*The Tornado*)

As shown in Figure 13 the 90 cm morphology of the Tornado is very similar to that seen at higher frequency (Stewart et al. 1994). Observations of maser emission from this source by Frail et al. (1996) and Yusef-Zadeh et al. (1999) supports its identification as an SNR. We are not able to present any quantitative results for Tornado because it is so far from the phase center that the primary beam attenuation is large and uncertain, resulting in considerable uncertainty in the measurement of its flux density.

4.8. *The Filaments and Threads*

The GC nonthermal filaments (hereafter referred to NTFs; for reviews, see Yusef-Zadeh 1989b; Morris 1996; Morris & Serabyn 1996) are magnetic structures emitting synchrotron radiation. As seen in Figure 1 all but one of the

NTFs (G358.87+0.47, § 4.9.1) are oriented perpendicular to the Galactic plane. The NTFs exhibit remarkable coherence and very large length-to-width ratios. However, the origin of these structures and the high-energy electrons responsible for their synchrotron emission is not clear. There is evidence that all the well-studied NTFs are associated and physically interacting with molecular gas. It has been hypothesized that fast moving clouds interacting with a large-scale magnetic field generates the observed phenomenology (e.g., Benford 1987; Lesch & Reich 1992; Serabyn & Morris 1994; Uchida et al. 1996; Staguhn et al. 1998; see Shore & LaRosa 1999 for an alternative but related model). We summarize here our insights into the nonthermal filaments inferred from our reprocessed 90 cm observations.

4.8.1. *Sgr C Filament*

The Sgr C filament was first studied by Liszt (1985). At 18 cm the filament appears to bifurcate into two subfilaments just beyond its midpoint located at $17^{\text{h}}44^{\text{m}}28^{\text{s}}$, $-29^{\circ}25'$. At this same location there is a definite peak in 90 cm intensity, suggesting that the peak in brightness occurs where several subfilaments appear to overlap.

Figure 14 shows our 90 cm image of Sgr C. Using the original 90 cm AB configuration data ($17''$ beam), Anantharamaiah et al. (1991) found that the spectral index was flat ($\alpha \approx 0.2$) near the eastern end of the filament and became progressively steeper going west along the filament ($\alpha \approx -0.9$ at the western end).

We have recalculated the spectral index using the reprocessed 90 cm BCD data ($43''$ beam). We have determined the

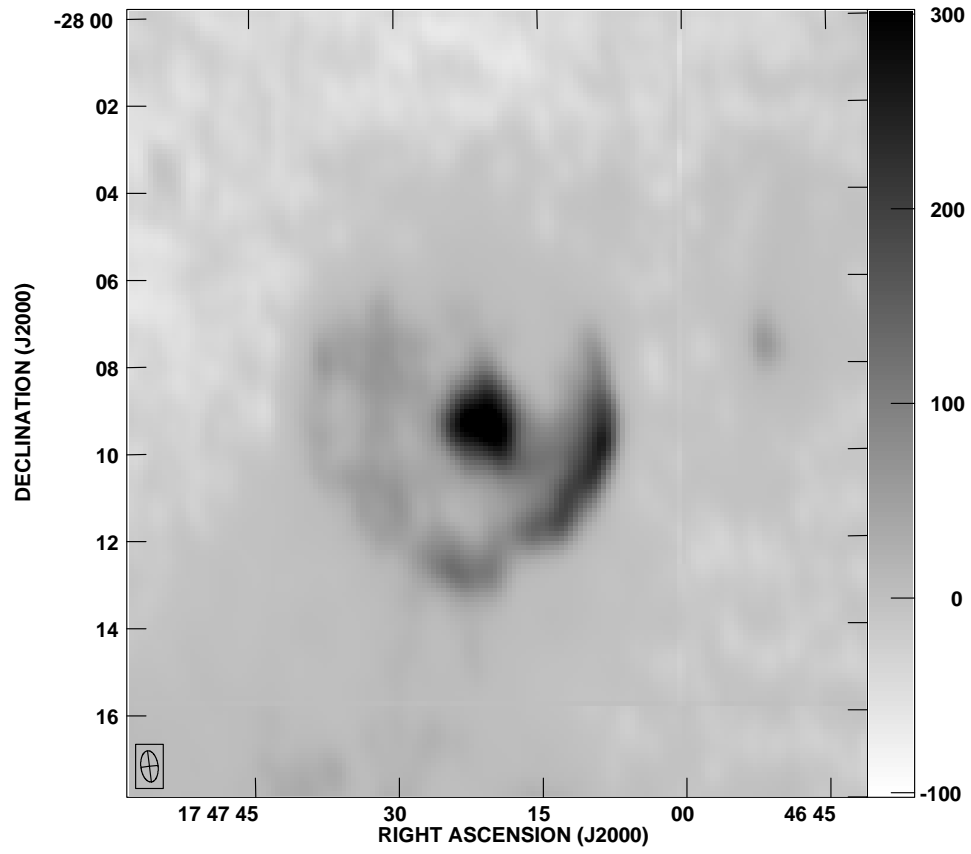


FIG. 8a

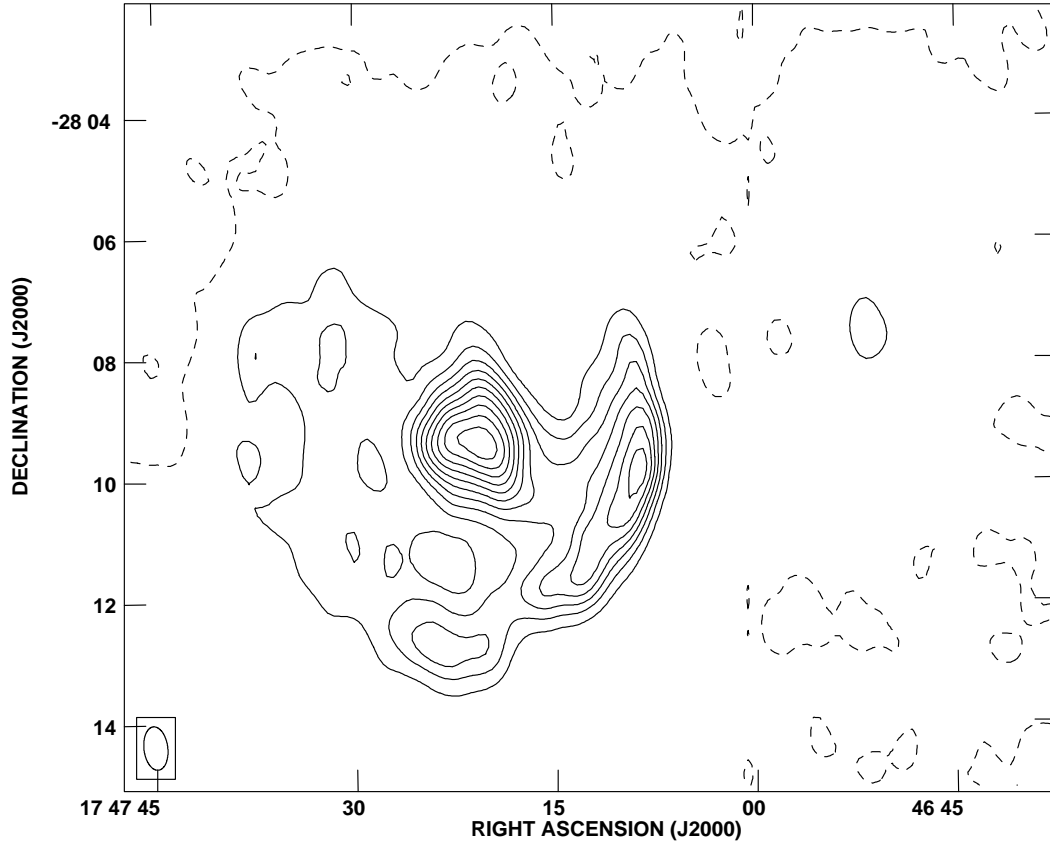


FIG. 8b

FIG. 8.—Images of G0.9+0.1. (a) Gray-scale levels are linear and in units of mJy beam⁻¹. (b) Contour levels are -30, 50, 100, 150, 200, 250, 300, 350, 400, 450, and 500 mJy beam⁻¹. The beam is shown in the lower left.

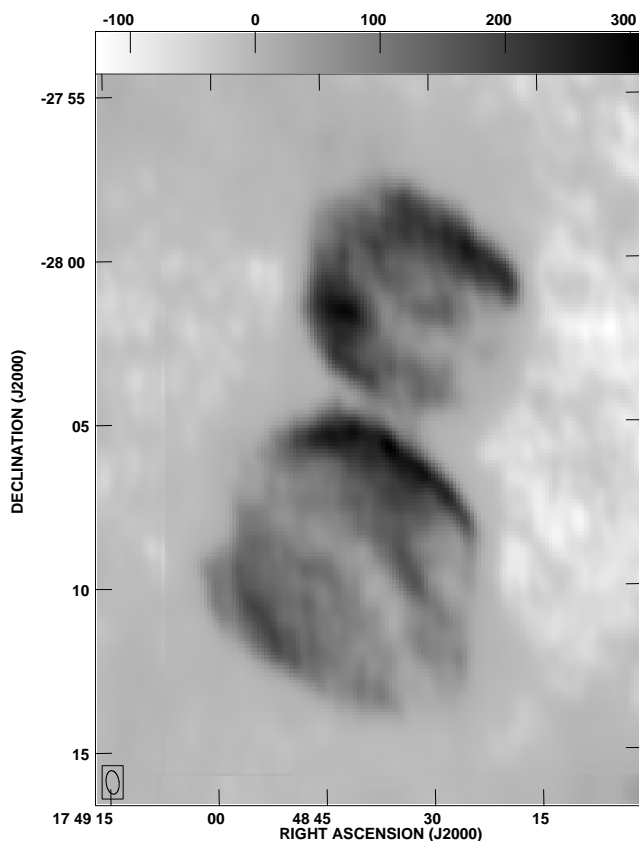


FIG. 9a

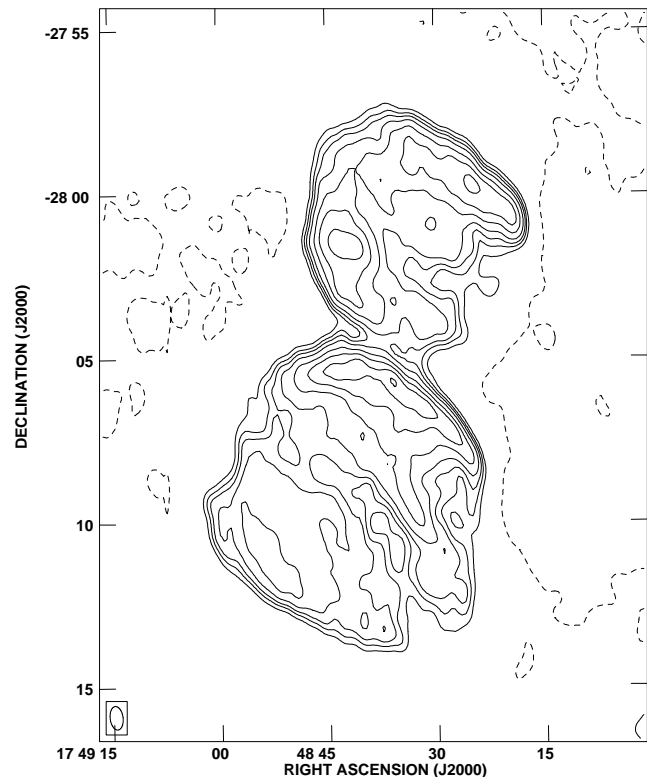


FIG. 9b

FIG. 9.—Images of Sgr D. The upper source is the H II region; the lower source is the supernova remnant. (a) Gray-scale levels are linear and in units of mJy beam⁻¹. (b) Contour levels are -30, 30, 50, 70, 100, 150, 200, 250, and 300 mJy beam⁻¹. The beam is shown in the lower left.

spectral index between 18 and 90 cm as a function of position along the filament by comparing peak brightnesses determined from crosscuts in the north-south direction. The 18 cm map of Liszt (1992) was convolved to the resolution of the 90 cm data before making the crosscuts. We recognize the potential errors inherent in comparing observations with different resolutions and (u, v) coverage, as well as different pointings, beam responses, and backgrounds. However, despite these conditions, our spectral-index results from a number of slices along the filament are remarkably consistent. Figure 15 shows the locations of the crosscuts and the spectral index derived at each crosscut location. Figure 16 shows the resulting spectral index as a function of position along the filament. The error bars in the figure were estimated from the uncertainty in determining the baselines for the individual slices. The spectral index at the far eastern end of the filament reflects the thermal emission from the Sgr C H II region; at this location the spectral index is flat with $\alpha \approx 0.02$.

Beyond the H II region the spectral index remains essentially constant at approximately -0.5 . In fact, the standard deviation of the 15 slices is 0.06. A constant spectral index is initially surprising since spectral aging may be expected from some of the models summarized above in which electrons are injected at the filament's eastern end where it crosses the H II region.

However, spectral steepening may not be observable in the filaments even if the electrons are injected at one end. The radio luminosity of the filament implies a minimum energy of order 10^{46} ergs and an equipartition magnetic

field of order 0.1 mG. This value is an order of magnitude lower than that derived from dynamical arguments applied to the filaments in general by Yusef-Zadeh & Morris (1987a, 1987b). For the equipartition field the synchrotron lifetime of electrons responsible for the 90 cm emission is of order 10^6 years. The observed length of the filament assuming it is located at the GC is 27 pc. Assuming the high-energy electrons stream at the Alfvén speed (Wentzel 1974) in a straight trajectory, electrons can easily traverse a length of several hundred pc in their lifetime. This is also true if one adopts the larger magnetic field, which gives a shorter lifetime but a larger Alfvén speed.

4.8.2. G0.08+0.15

This filament is located just north of Sgr A East and is south of the GCRA (Fig. 17). It is referred to as the northern thread (Morris & Yusef-Zadeh 1985). It runs through the arched filaments and almost merges with the diffuse GCRA emission at its far northern extension. Whereas high-frequency observations show a fairly uniform surface brightness, at 90 cm this filament is clearly brighter at the midpoint location ($17^{\text{h}}45^{\text{m}}14^{\text{s}}$, $-28^{\circ}47'$). At high resolution it is extremely narrow. It is resolved at 6 cm to be $4''$, which corresponds to 0.15 pc (Lang, Morris, & Echevarria 1999b). Beyond the arched filaments it has a linear extent of 11.9 at 90 cm, corresponding to a length of at least 29.4 pc at the GC.

The integrated 90 cm flux density of this filament in the region beyond the arched filaments is 7.5 Jy, which corresponds to a radio luminosity of 3×10^{33} ergs s⁻¹. A

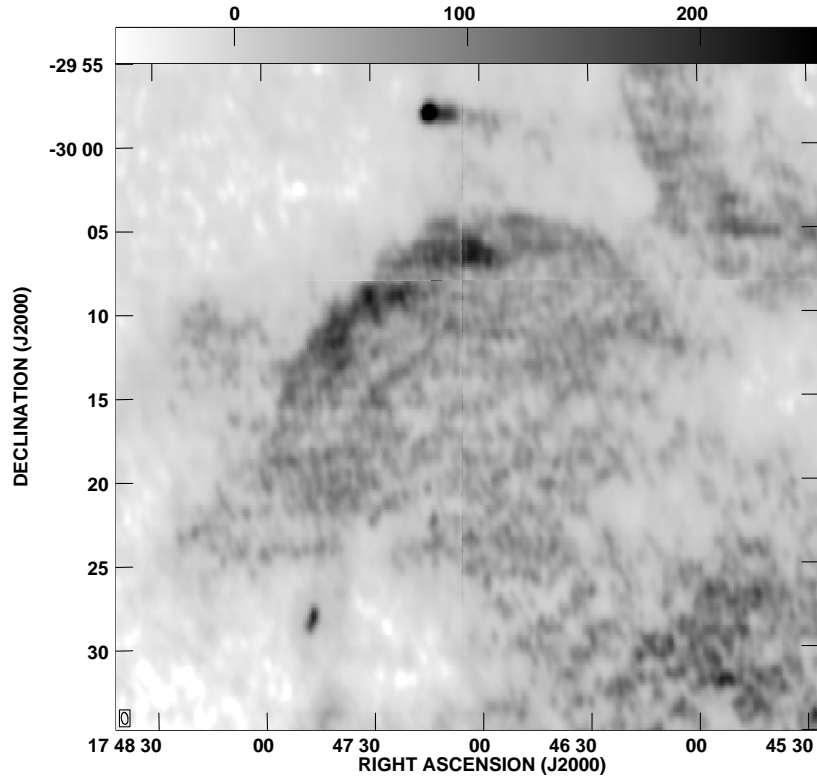


FIG. 10a

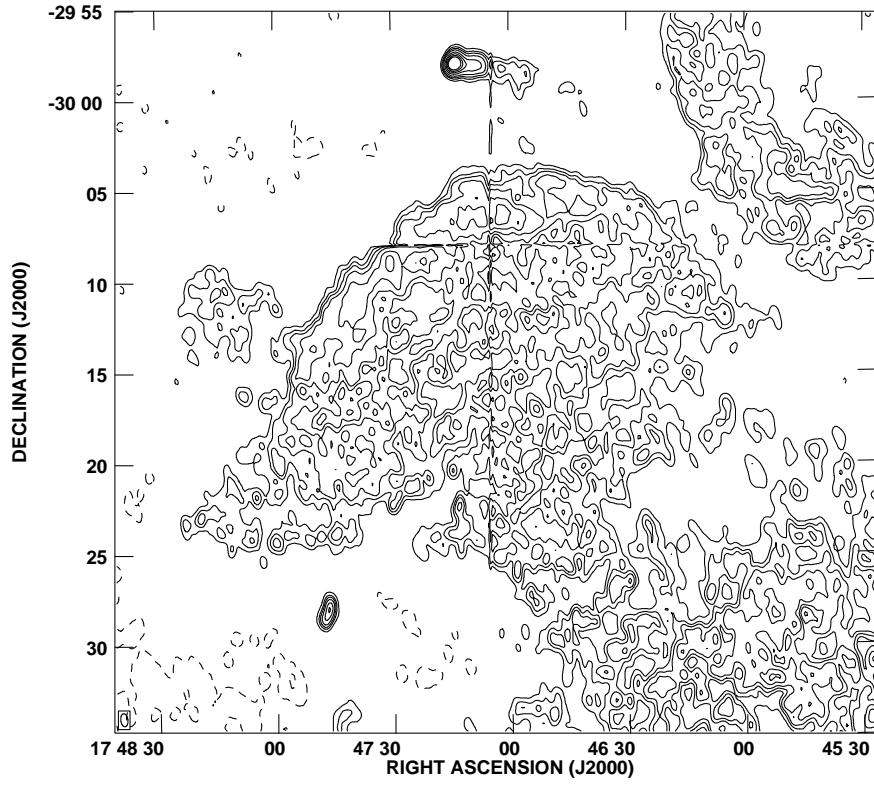


FIG. 10b

FIG. 10.—Images of G359.0—0.9. The bright source at the top of both figures is the Mouse (Fig. 12). (a) Gray-scale image. Gray-scale levels are linear and in units of mJy beam⁻¹. (b) Contour image. Contour levels are -30, 30, 50, 70, 100, 150, 200, 250, and 300 mJy beam⁻¹. The beam is shown in the lower left.

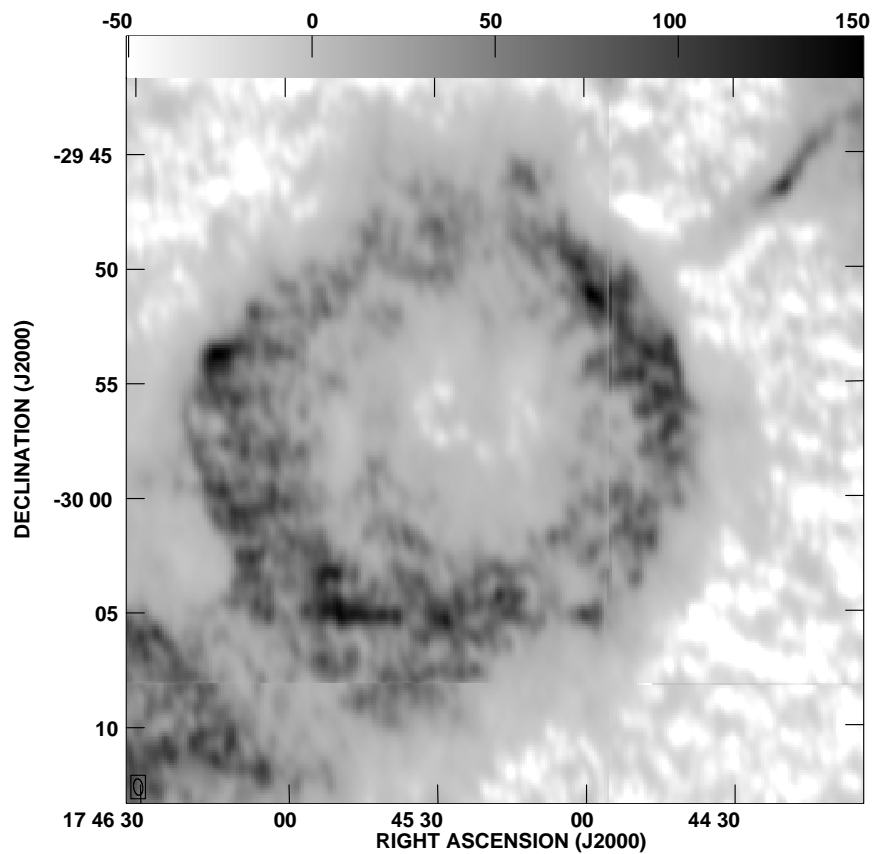


FIG. 11a

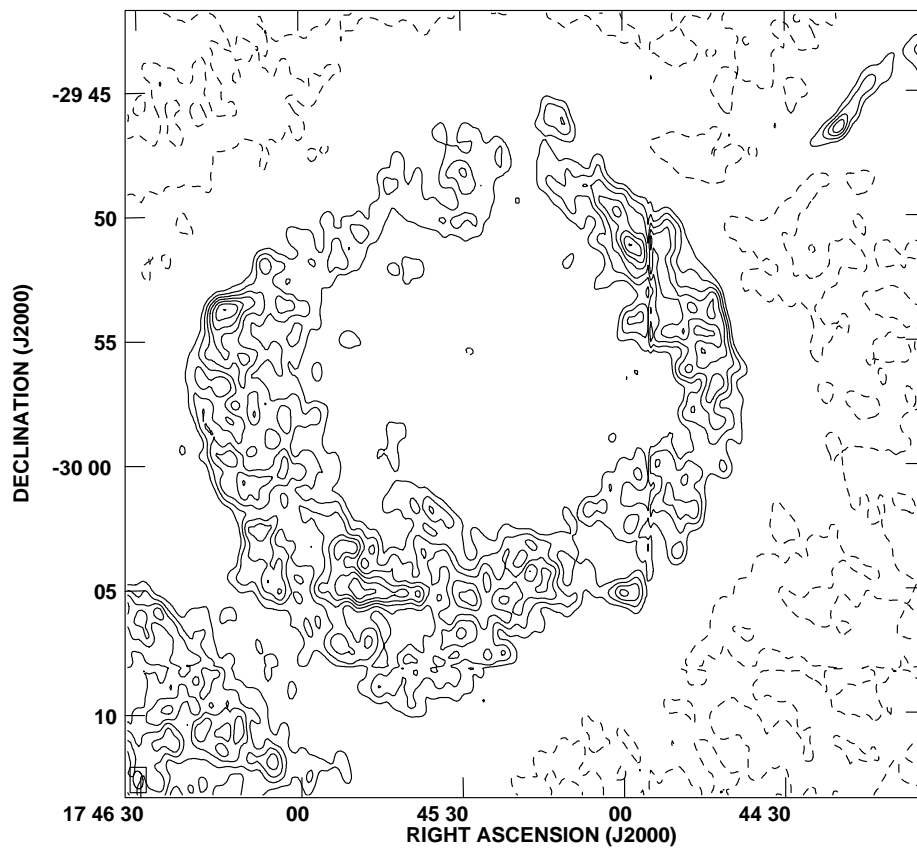


FIG. 11b

FIG. 11.—Images of G359.1–0.5. The Snake (Fig. 23) is also visible in the northwest. (a) Gray-scale levels are linear and in units of mJy beam^{-1} . (b) Contour levels are $-30, 30, 50, 70, 90, 110, 130$, and $150 \text{ mJy beam}^{-1}$. The beam is shown in the lower left.

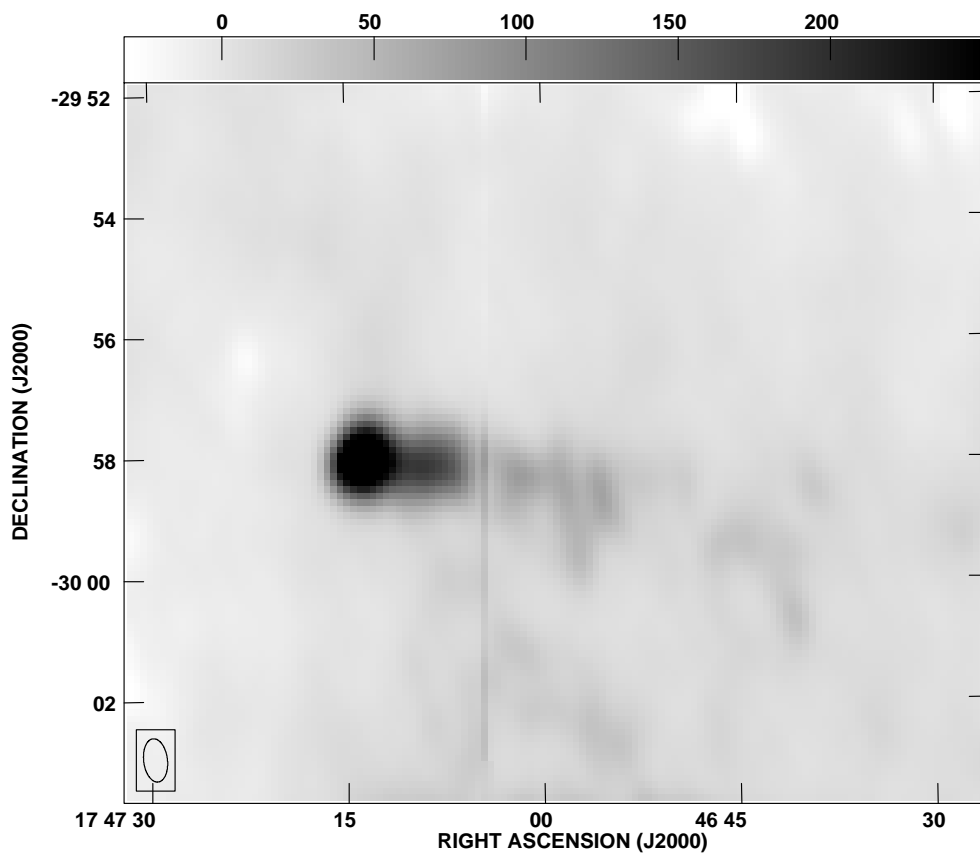


FIG. 12a

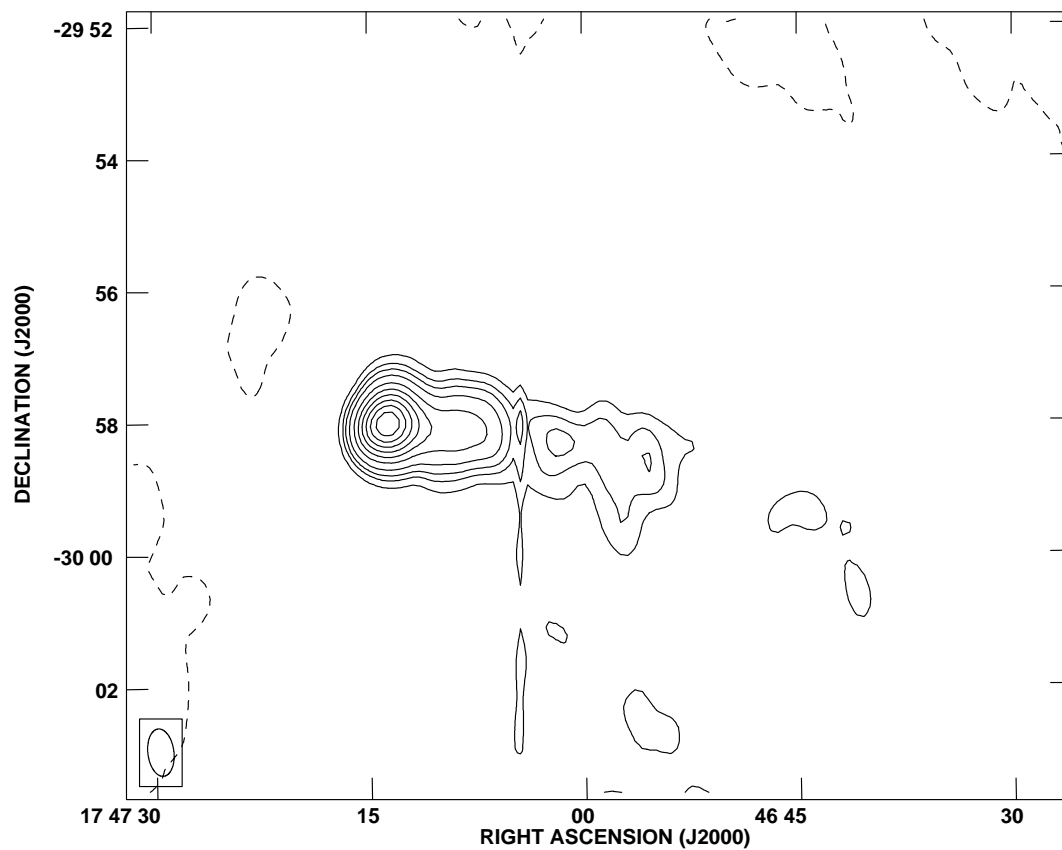


FIG. 12b

FIG. 12.—Images of G359.3–0.82, the Mouse. (a) Gray-scale levels are linear and in units of mJy beam^{-1} . (b) Contour levels are $-10, 30, 50, 70, 100, 150, 200, 250, 300, 350$, and $400 \text{ mJy beam}^{-1}$. The beam is shown in the lower left.

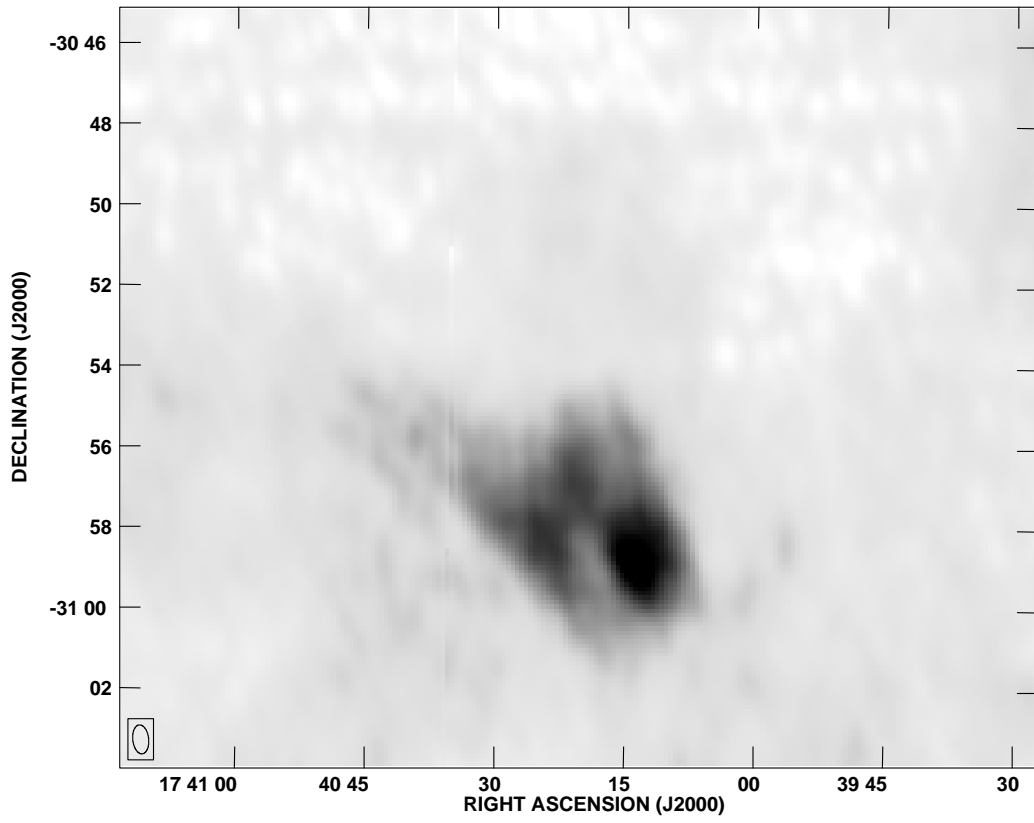


FIG. 13a

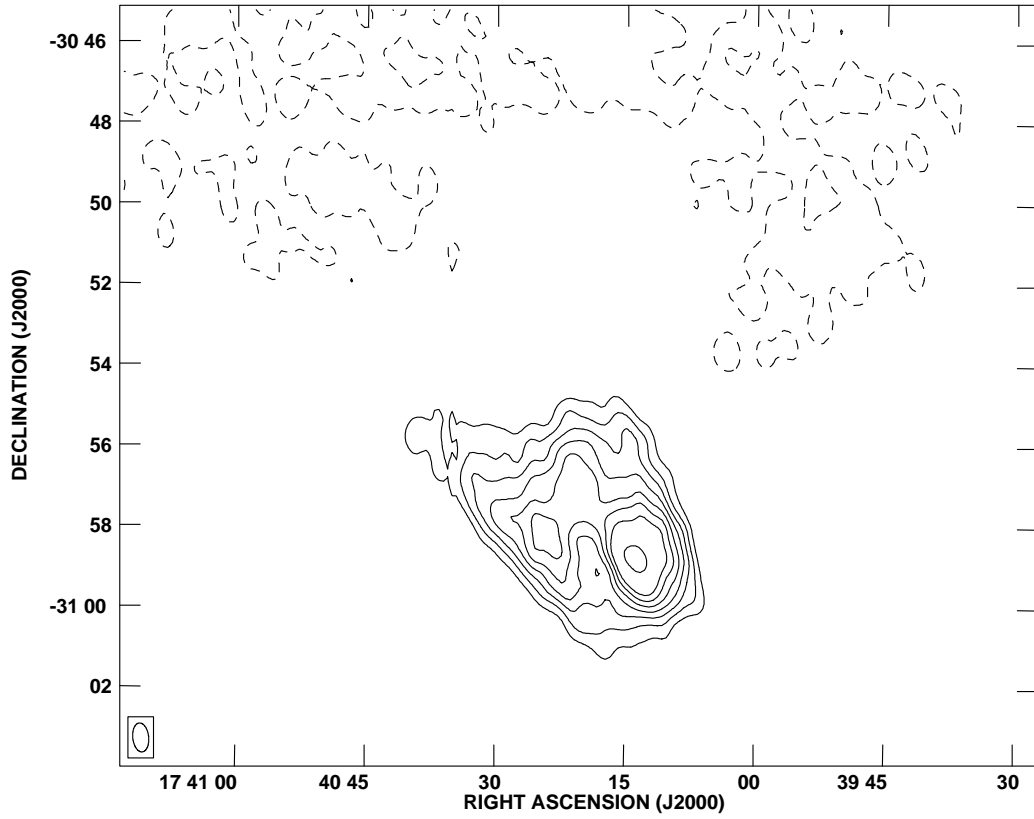


FIG. 13b

FIG. 13.—Images of G357.7–0.1, the Tornado. These images have not been corrected for primary-beam attenuation due to its location at the extreme edge of the field of view. (a) Gray-scale levels are linear and in units of mJy beam^{-1} . (b) Contour levels are $-10, 30, 50, 70, 90, 110, 130, 150,$ and $200 \text{ mJy beam}^{-1}$. The beam is shown in the lower left.

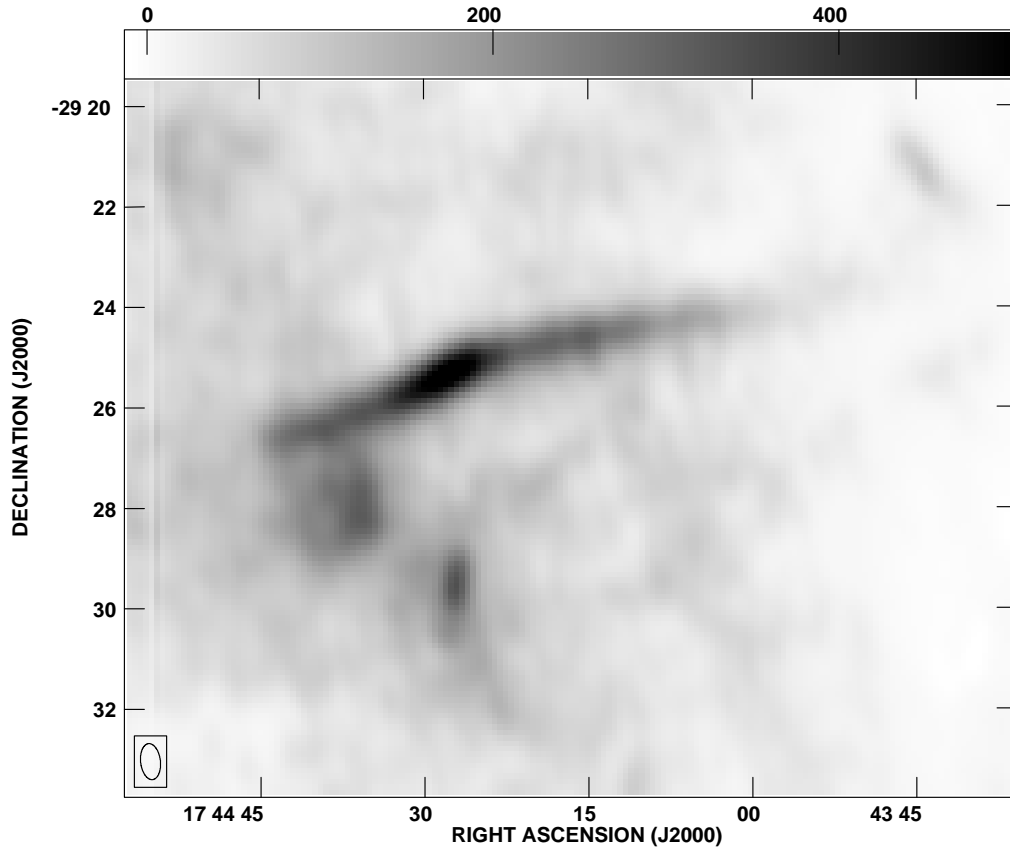


FIG. 14a

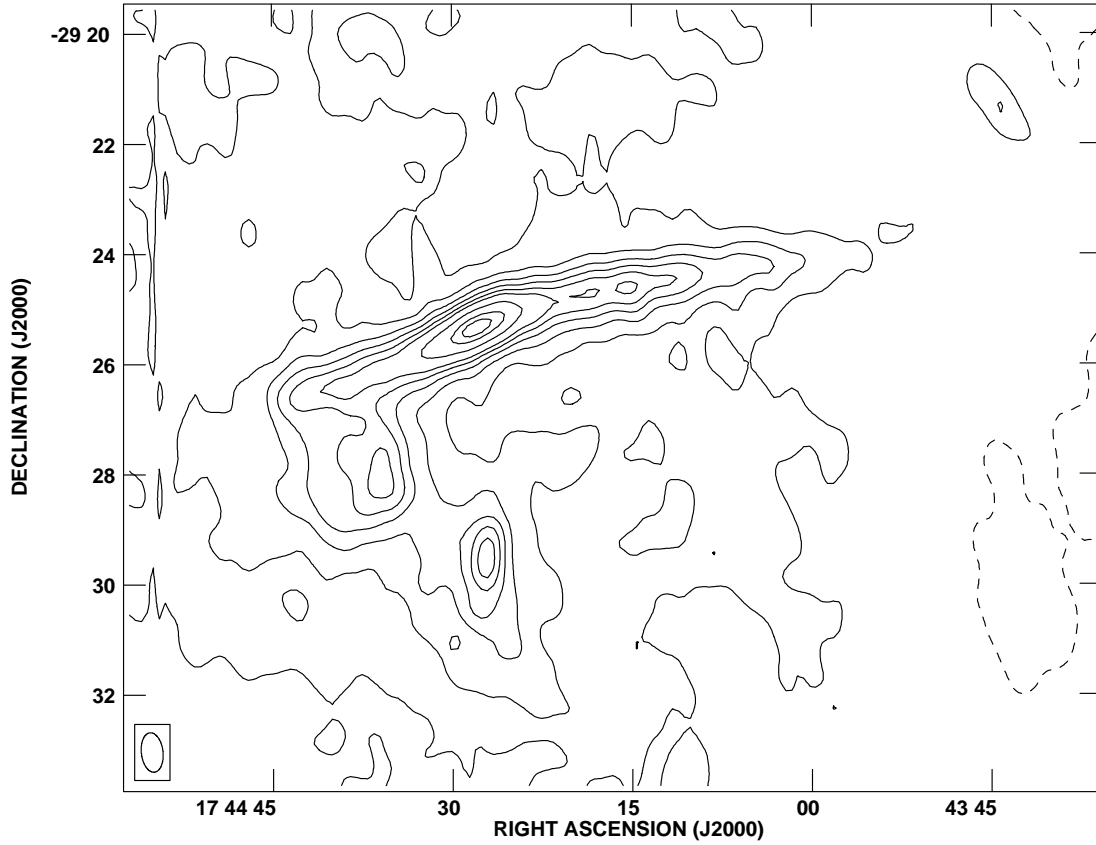


FIG. 14b

FIG. 14.—Images of the Sgr C filament. (a) Gray-scale levels are linear and in units of mJy beam^{-1} . (b) Contour levels are $-10, 50, 100, 150, 200, 250, 300, 400, 500$, and $550 \text{ mJy beam}^{-1}$. The beam is shown in the lower left.

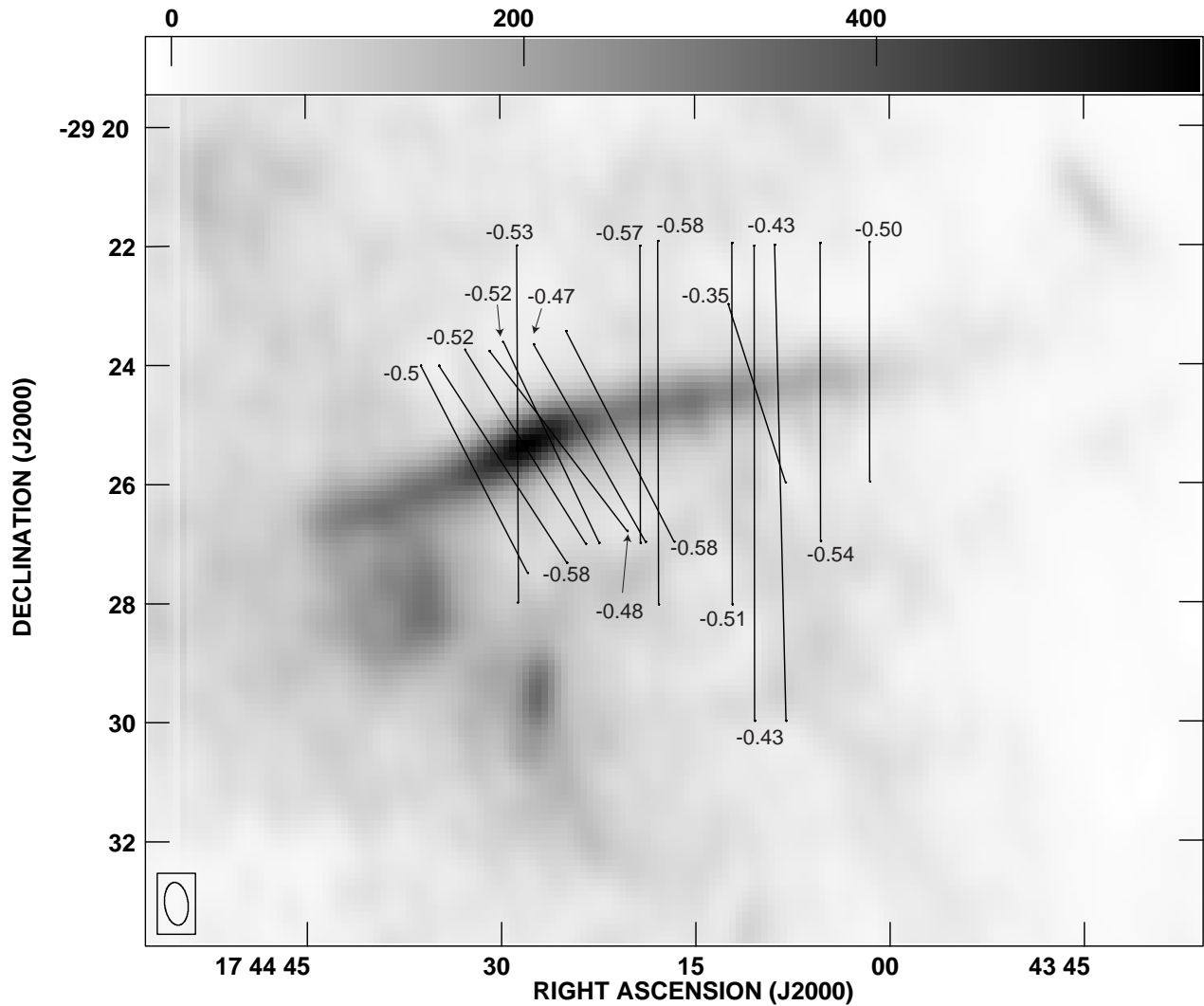


FIG. 15.—Location of cross-cuts taken through the Sgr C filament used in determining the spectral index as a function of position along the filament (Fig. 16). The number associated with each cross cut is the spectral index at that location. The gray-scale levels are in mJy beam^{-1} . The beam is shown in the lower left.

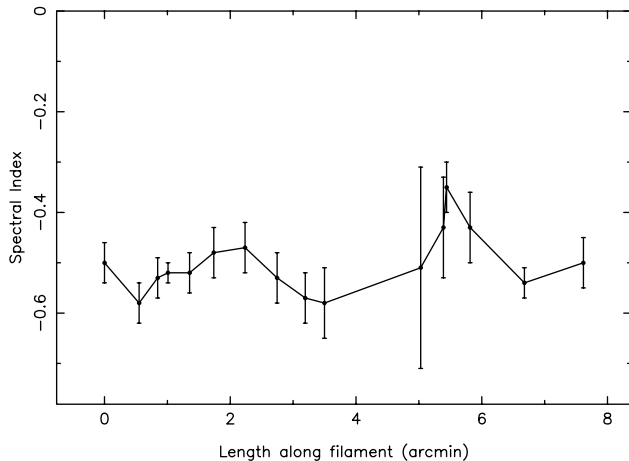


FIG. 16.—Spectral index as a function of position along the Sgr C filament. Error bars were estimated from uncertainties in the baselines for the individual slices.

minimum energy analysis yields an energy requirement of 9×10^{46} ergs and a magnetic field of strength of 0.1 mG. The spectral index between 20 and 90 cm as a function of length along the filament has been estimated using the 20 cm data of (Lang et al. 1999b). As with the Sgr C filament, the index was determined by first convolving the 20 cm data to the 90 cm resolution. We then made crosscuts perpendicular to the filament and compared the peak fluxes along the filament. Unlike the Sgr C filament, owing to a lack of short spacings and proximity to the Sgr A complex, the northern and southern (see below) threads are located in a deep negative flux bowl. This bowl complicates the spectral index determination, and the error bars are larger than for the Sgr C filament. Figure 18 shows the resulting spectral indices as a function of position along the thread. Within the errors the results suggest and are consistent with a constant spectral index of -0.6 . This agrees with the constancy of the spectral index between 6 and 20 cm found by Lang et al. (1999b), but, similar to Sgr C, the long synchro-

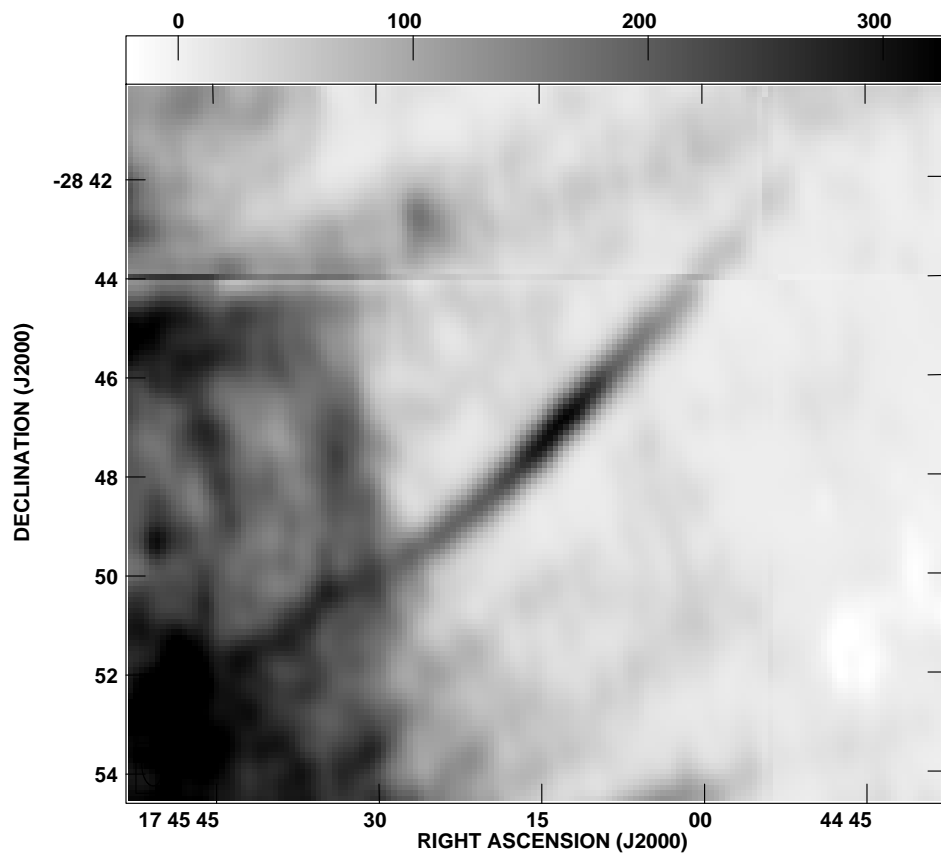


FIG. 17a

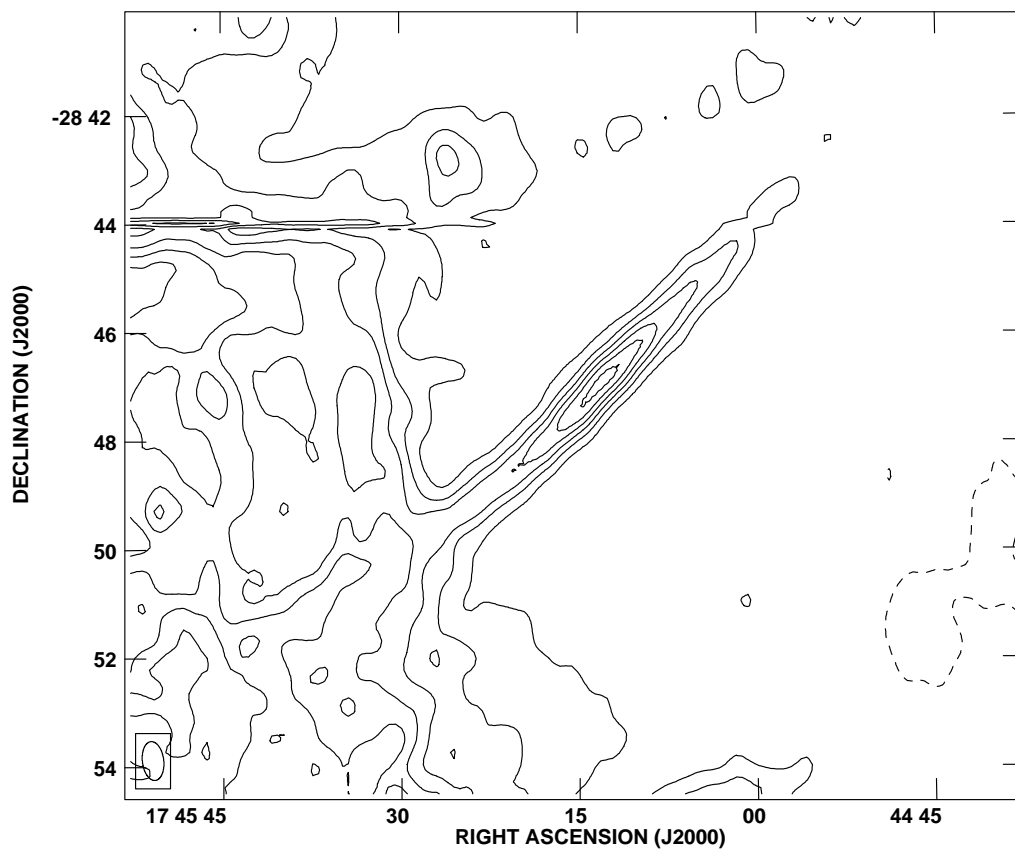


FIG. 17b

FIG. 17.—Images of the filament G0.08+0.15. (a) Gray-scale levels are linear and in units of mJy beam^{-1} . (b) Contour levels are $-10, 50, 100, 150, 200, 250, 300$, and $350 \text{ mJy beam}^{-1}$. The beam is shown in the lower left.

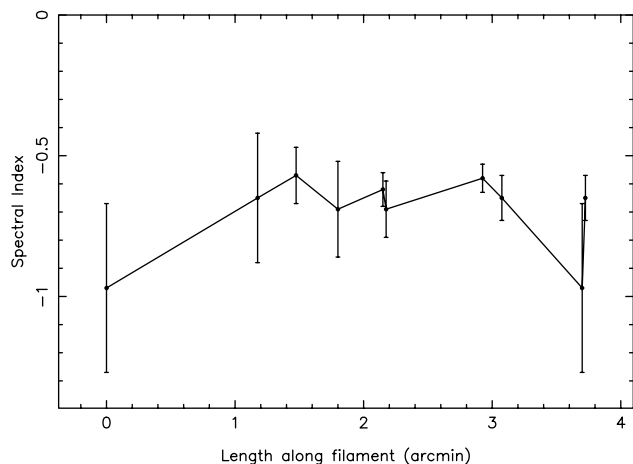


FIG. 18.—Spectral index as a function of position along the northern thread G0.08+0.15. Error bars were estimated from uncertainties in the baselines of the individual slices.

tron lifetime may explain the absence of spectral aging. The constancy of spectral index is surprising in light of the clear brightness and structural variations along the filaments. At 20 cm the filament appears to feather into multiple strands and widens to 0.5 pc at its northern end.

4.8.3. G359.96+0.09

This filament, known as the southern thread, connects to and appears to emanate from the Sgr A complex (Fig. 19). At 90 cm the filament ends at about $17^{\text{h}}45^{\text{m}}00^{\text{s}}$, but at 20 cm the thread is observed to continue another $25'$, extending past the extragalactic source G359.87+0.18 (Lang et al. 1999b). This suggests that surface brightness sensitivity may be limiting the 90 cm observations. The surface brightness of this filament, unlike that of G0.08+0.15, is fairly constant at 90 cm. At 20 cm this thread also shows considerable substructure consisting of several distinct filaments braided together. As with the previous filaments, we have determined the spectral index between 20 and 90 cm as a function of length, using perpendicular crosscuts and comparing peak fluxes. Figure 20 shows that, although limited to only a few points along the filament by the low signal-to-noise ratio at 20 cm, the spectral index is consistent with a constant value of $\alpha \sim -0.6$. As with G0.08+0.15 the negative flux bowl leads to larger baseline errors. Previous estimates (Anantharamaiah et al. 1991) indicated a flat index for this source. However, -0.6 is consistent with the nonthermal nature of the NTFs. A minimum energy analysis yields parameters similar to G0.8+0.15, an energy requirement of order 10^{46} ergs, and a magnetic field of order 0.1 mG.

4.8.4. G359.79+0.17

Figure 21 shows this source to be an isolated filament that appears as a crescent shape at 90 cm. It is clearly seen at 20 cm to bifurcate into to at least two major strands (Yusef-Zadeh & Morris 1987a; Yusef-Zadeh & Morris 1987b; Lang et al. 1999b). Similar to G0.08+0.15 at 90 cm, this filament has its highest intensity near its midpoint ($17^{\text{h}}44^{\text{m}}30^{\text{s}}$, $-29^{\circ}01'30''$). Its length at 90 cm is approximately 15 pc.

4.8.5. G359.54+0.18

Figure 22 shows that this source is another example of an apparently isolated filament. It is considerably shorter than

the others, extending only 12 pc. Yusef-Zadeh, Wardle, & Parastaran (1997) have established that this is indeed a magnetic structure with a high degree of polarization. They have also shown that at 6 cm the source consists of several subfilaments that overlap near its midpoint ($17^{\text{h}}43^{\text{m}}50^{\text{s}}$, $-29^{\circ}14'$). It clearly has an intensity peak at its midpoint at 90 cm. Staguhan et al. (1998) have suggested that this filament is interacting with two molecular clouds, one at its extreme eastern end and the other offset to the east of the peak brightness. It is not clear why the intensity does not peak at the locations where the clouds are presumably interacting with the filament.

4.8.6. G359.1-0.2 (The Snake)

The Snake is an unusual NTF first noticed in the MOST (843 MHz) Galactic center survey (Gray et al. 1991, 1995). It is the only filament that has abrupt changes in direction or kinks. At 20 and 35 cm the Snake is also the longest NTF, traversing a distance of roughly 60 pc (assuming it is located at the GC; Uchida et al. 1992) between a diffuse region of emission situated in the Galactic plane through the non-thermal shell source G359.1-0.05.

Figure 23 shows that at 90 cm the Snake appears considerably shorter, only extending halfway to G359.01-0.05. The Snake shows a marked change in thickness at 20 cm at the location where it disappears on our 90 cm image. Over the western half the Snake is 2 to 3 times thicker than over its eastern half. At 90 cm the thin part of the Snake is not detected, presumably because of surface brightness sensitivity.

4.8.7. Filament Summary

There are several characteristics common to most of the NTFs observed at 90 cm.

1. With the exception of the southern thread, the peak brightness occurs near the midpoint or geometric center of the filaments.
2. At higher resolution the midpoints also coincide with locations where subfilaments appear to overlap and braid together into multiple filaments.
3. For the three filaments with corresponding 20 cm data we find no evidence for a change in spectral index with length along the filaments. This result, however, does not contradict the scenario that energetic electrons are fed into the filament at one end since the synchrotron lifetime may be long enough to prevent detection of spectral aging.

4.9. New Extended Sources

4.9.1. G358.85+0.47 (The Pelican)

The linear source G358.85+0.47 (Fig. 24), located approximately a degree (~ 150 pc in projection) southwest of Sgr A, was first noticed and discovered on Figure 1 because of its similar appearance to the isolated NTFs (Kassim et al. 1999). Follow-up observations of this source by Anantharamaiah et al. (1999) and Lang et al. (1999a) at shorter wavelengths have confirmed that this source is non-thermal and displays the same filamentary structure as do the other NTFs. The identification of this source as an NTF highlights the importance of wide-field, three-dimensional imaging at low frequencies. At higher frequencies its appearance is that of several subfilaments that join or inter-

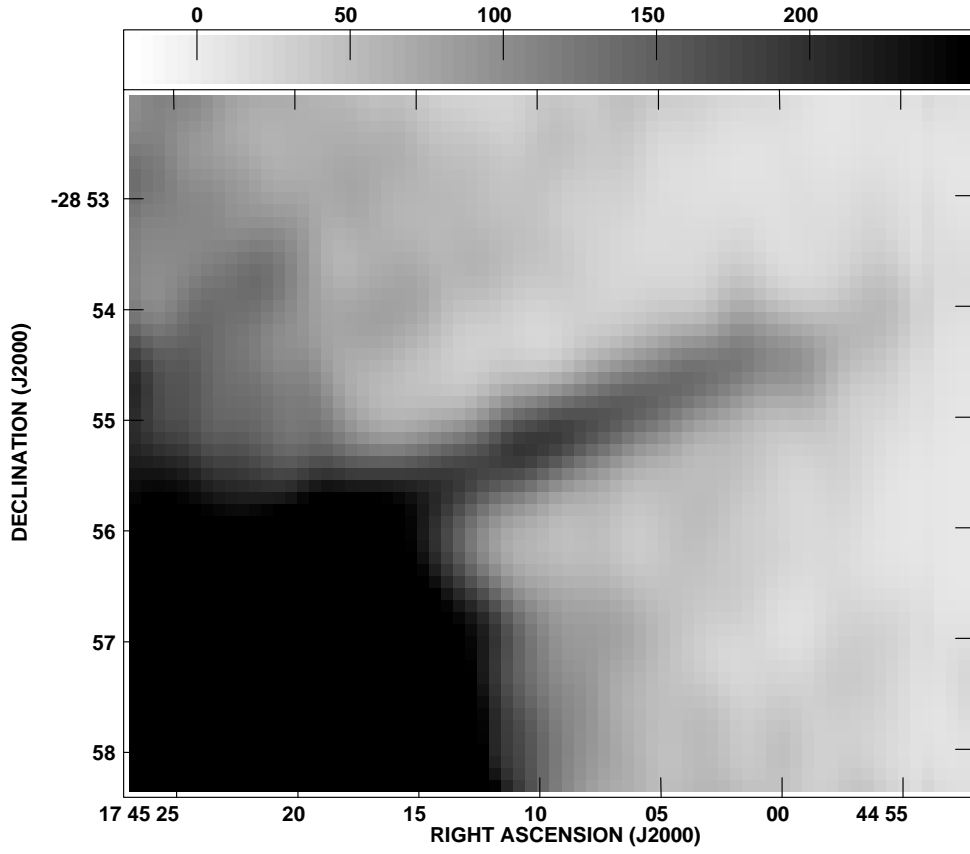


FIG. 19a

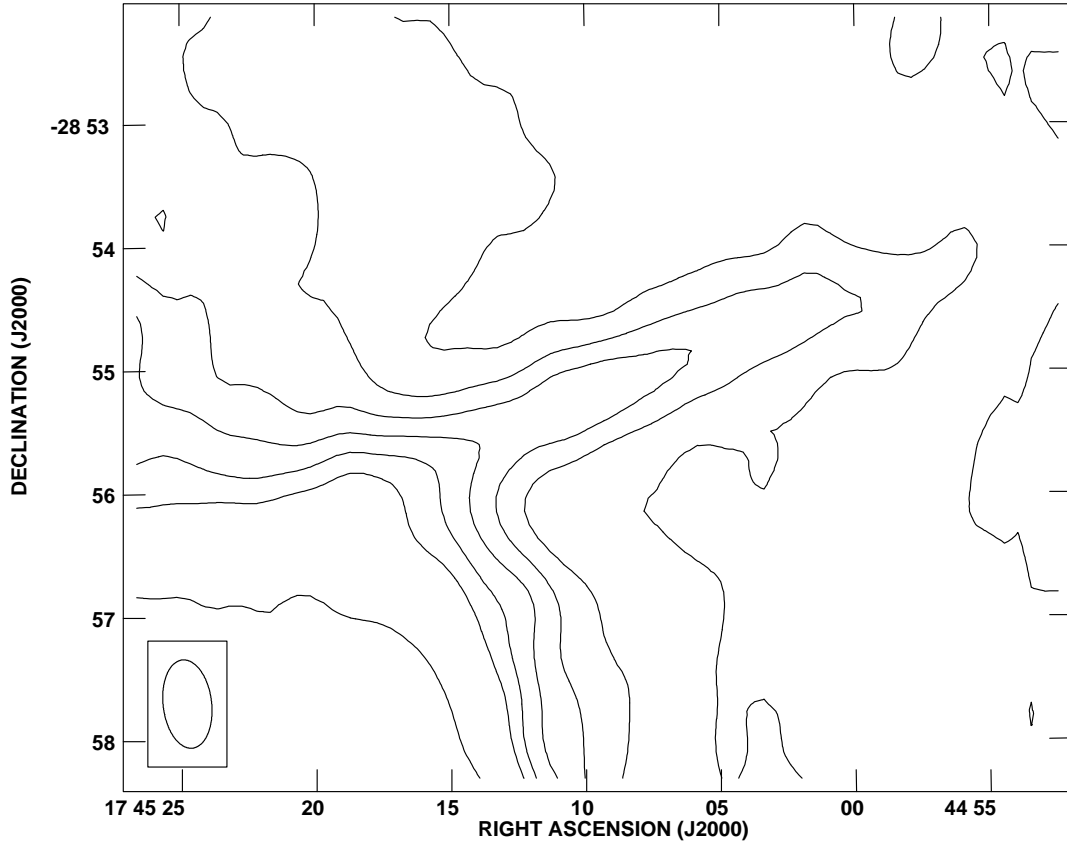


FIG. 19b

FIG. 19.—Images of the filament G359.96+0.09. (a) Gray-scale levels are linear and in units of mJy beam^{-1} . (b) Contour levels are $-5, 10, 50, 100, 150, 200, 250, 300,$ and $500 \text{ mJy beam}^{-1}$. The beam is shown in the lower left.

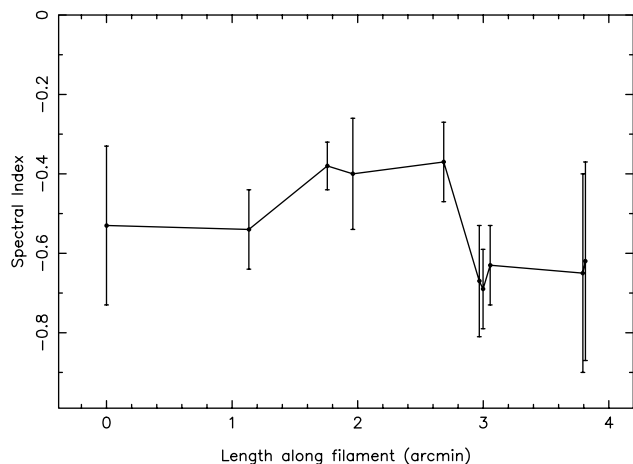


FIG. 20.—Spectral index as a function of position along the southern thread G359.96+0.09. Error bars were estimated from uncertainties in the baselines of the individual slices.

sect near its center, where the 90 cm emission is most intense.

It has been suggested (Morris 1994) that the NTFs trace a large-scale magnetic field. If so, the orientation of G358.85+0.47 parallel to the Galactic plane indicates that the field must diverge quite rapidly. Closer to Sgr A, the NTFs are all oriented perpendicular to the Galactic plane, suggesting that the field is dominated by perpendicular components.

4.9.2. G359.85+0.39

Figure 25 shows the source we have named “the Cane.” It is an unusual region of extended emission located 12' (~ 30 pc in projection) due west from Sgr A. This source is shaped like a cane with a wide handle. The linear part extends for 7' and then bends into a semicircular half shell. At this resolution it appears to be a contiguous structure. Follow-up observations of this source are underway.

4.9.3. G359.92–1.03

Figure 26 shows a third extended feature, G359.92–1.03, that is located on the opposite side of the Galactic plane from the NTFs. It appears about 146 pc in projection from Sgr A. It is also a linear feature similar to G358.85+0.47, but it is inclined at an angle of 60° to the Galactic plane. Follow-up observations of this source are also underway. If it is a NTF, it would be the first found on the negative latitude side of the plane and may be the only tracer of the magnetic field at southern latitudes in the GC.

4.9.4. G359.07–0.02

Figure 27 shows this large-scale feature located on and elongated parallel to the Galactic plane near Sgr E. The source is not distinct in higher frequency surveys, and at low resolution it could be easily be taken for background thermal emission. However, it is seen on the 35 cm survey of the Galactic center region by Gray (1994a). Curiously, the spatial structure of this source is very similar to both Sgr A East and G0.3+0.0 although its brightness is much lower. Its shape is reminiscent of barrel-shaped SNRs (e.g., Gaensler 1998). The major axis of most barrel or bilateral SNRs is aligned along the galactic plane. We therefore speculate that this source is indeed a SNR. Additional observations at

other wavelengths are needed to determine the nature of this source.

5. SMALL-DIAMETER SOURCES

Figures 28 and 29 show the latitude and spectral index distributions of the small-diameter sources we have identified. The spectral index distribution shows only those 42 sources with an NVSS counterpart.

The mean spectral index of our sources with known spectral indices is -0.84 ± 0.10 . This mean spectral index is relatively steep because we have few sources with “flat” spectral indices ($\alpha > -0.25$). Figure 28 shows that the sources with nonthermal spectral indices ($\alpha < -0.25$) have a distribution that is nearly constant with latitude, though there may be a slight concentration of nonthermal sources toward the Galactic plane. These nonthermal sources are probably dominated by extragalactic sources, though their number includes at least one pulsar (PSR B1749–28, G1.54–0.96) and could include young or distant SNRs.

The density of SNRs is known to increase toward the GC (Gray 1994b), and they have a scale height of approximately 0.9 (130 pc at 8.5 kpc, Becker et al. 1990). The spectra of our small-diameter sources is slightly steeper than the nominal spectrum of SNRs in the Galactic disk in the range -0.5 to -0.7 (Reynolds 1988). This discrepancy may be due to environmental effects, though, as there are indications that SNRs in the GC may have steeper spectral indices than those in the Galactic disk (e.g., G0.3+0.0, Kassim & Frail 1996). By the same token, the diameters of these sources, 1–2 pc, are probably smaller than SNRs of a comparable age in the Galactic disk. Densities in the GC can be easily 10^3 – 10^5 times higher than those in the Galactic disk, meaning that SNRs in the Sedov phase of their expansion would be 4 to 10 times smaller than those in the Galactic disk.

Anantharamaiah et al. (1991) suggested that there would be a population of extragalactic radio sources seen through the GC. The enhanced interstellar angular broadening toward the GC undoubtedly broadens some sources to the point of being undetectable. However, the most intense broadening is localized to the inner $45'$ or so and is patchy (Lazio & Cordes 1998; Lazio et al. 1999), allowing a number of extragalactic sources to remain detectable.

The small-diameter sources with unknown spectral indices could be a mixture of both known Galactic radio source populations—SNRs, H II regions, planetary nebulae, radio pulsars, and radio stars—and extragalactic radio sources. The strong concentration toward the Galactic plane seen in the bottom panel of Figure 28 indicates that at least one Galactic radio source population contributes to a substantial fraction of our sources with unknown spectral indices. Indeed, we expect the actual distribution to be even more concentrated toward the Galactic plane, as many sources in the Galactic plane have presumably gone undetected because of the intense emission from the Galactic ridge. Of the 78 sources we have detected, nineteen are toward the central region of our image, where confusion in the NVSS survey makes it difficult to identify a counterpart.

A significant number of the Galactic sources with unknown spectral indices are probably H II regions. Becker et al. (1990) and Becker et al. (1994) showed that H II regions are concentrated toward the Galactic plane with a (FWHM) width in Galactic latitude of 0.3° . The concentration toward the Galactic plane in the bottom panel of

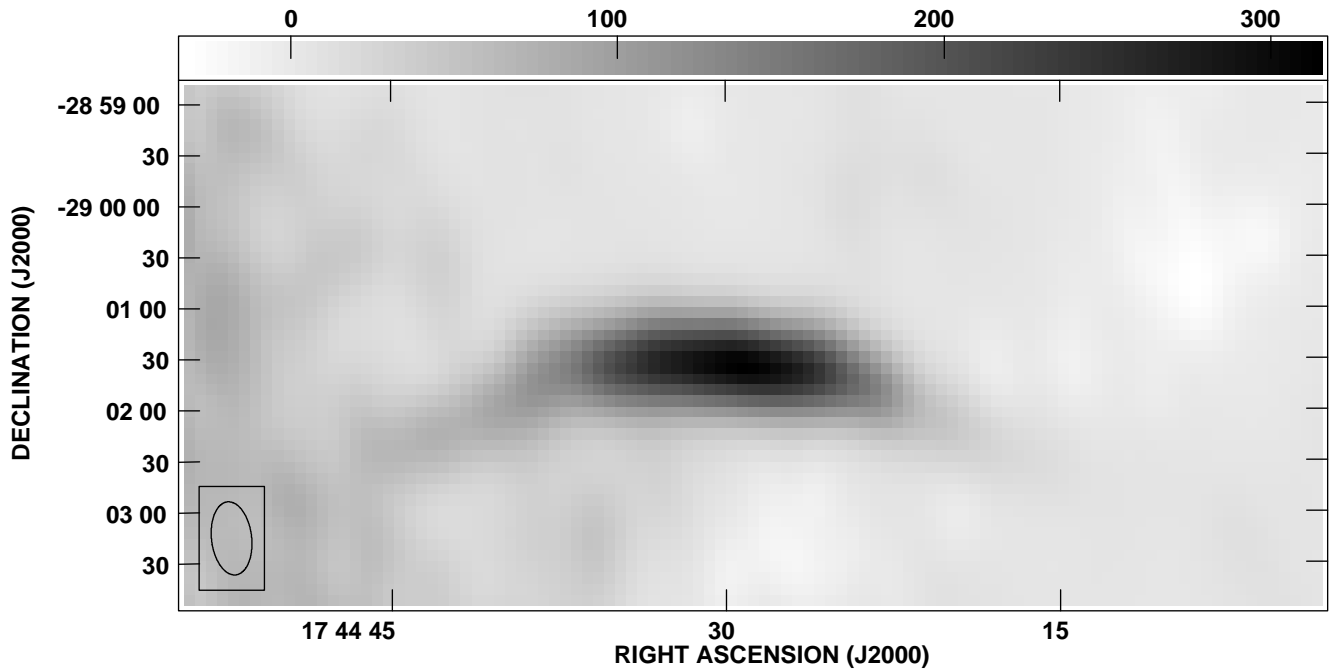


FIG. 21a

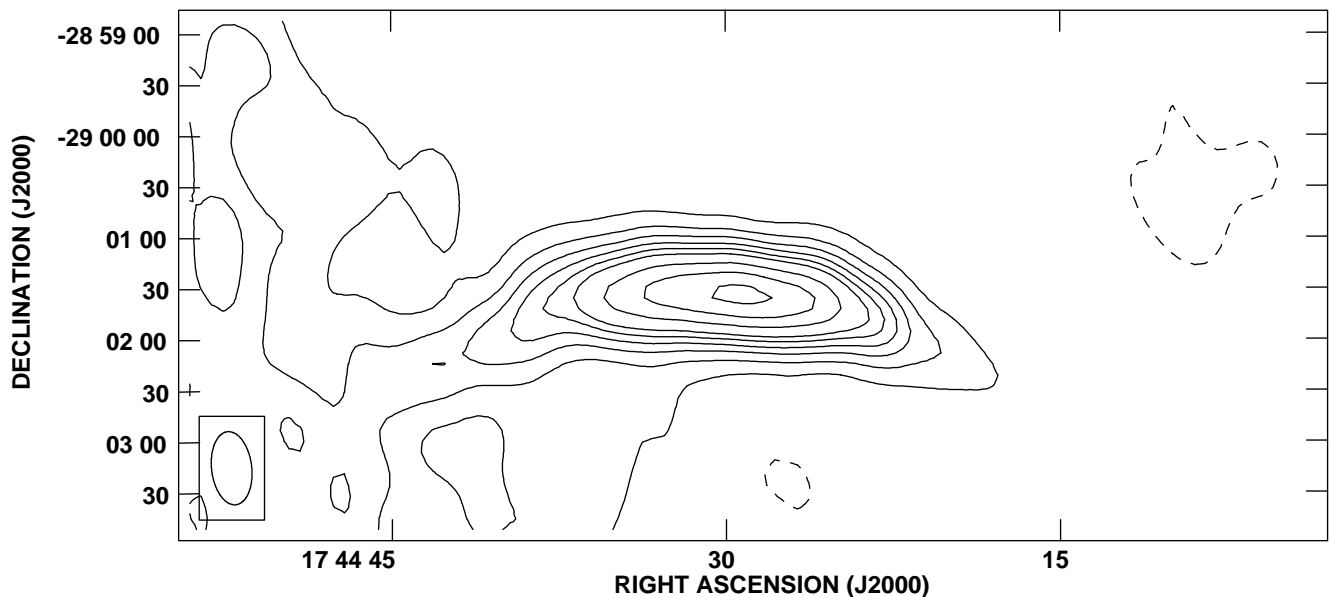


FIG. 21b

FIG. 21.—Images of the filament G359.79+0.17. (a) Gray-scale levels are linear and in units of mJy beam^{-1} . (b) Contour levels are $-15, 25, 50, 75, 100, 125, 150, 200, 250$, and $300 \text{ mJy beam}^{-1}$. The beam is shown in the lower left.

Figure 28 has a similar width. Moreover, there are 10 sources whose location near the center makes it difficult to identify an NVSS counterpart. These sources are either within Sgr B2 (three sources) or have an IRAS counterpart (four sources) or both (three sources) and are almost certainly H II regions. Thus, a substantial fraction of the sources with unknown spectral indices are likely to be H II regions.

6. DISCUSSION AND CONCLUSIONS

We have successfully imaged archival 90 cm VLA Galactic center data, using a wide-field algorithm that properly

compensates for the non-coplanar baseline effects encountered at long wavelengths. This has allowed us to image a larger field of view than previously possible with these data, and to obtain increased image fidelity and sensitivity across most of the map. This has resulted in one of the largest and most sensitive high-resolution, long-wavelength images of this unique region.

A systematic examination of this new image has resulted in a catalog of over a hundred sources. Several new sources of extended emission have been identified, including a new nonthermal filament that is parallel to the Galactic plane. We have estimated the spectral index as a function of length

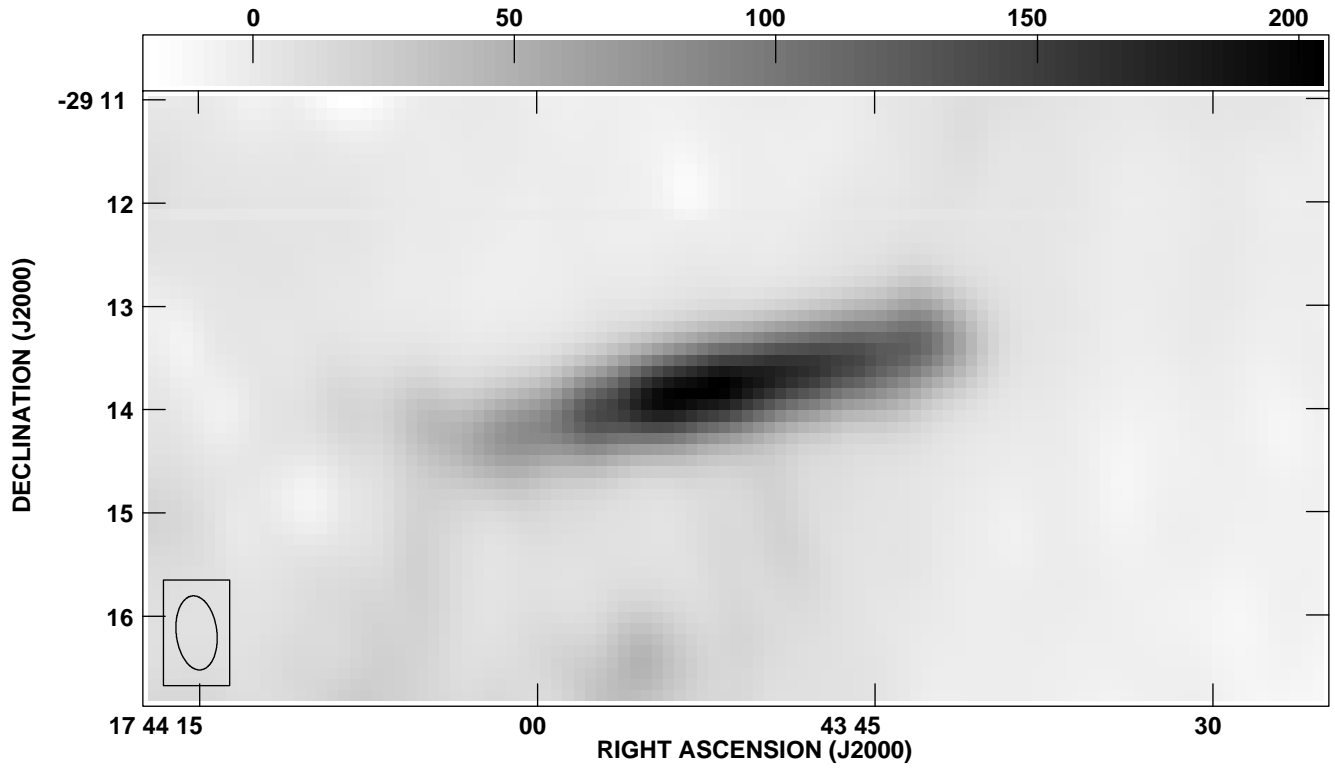


FIG. 22a

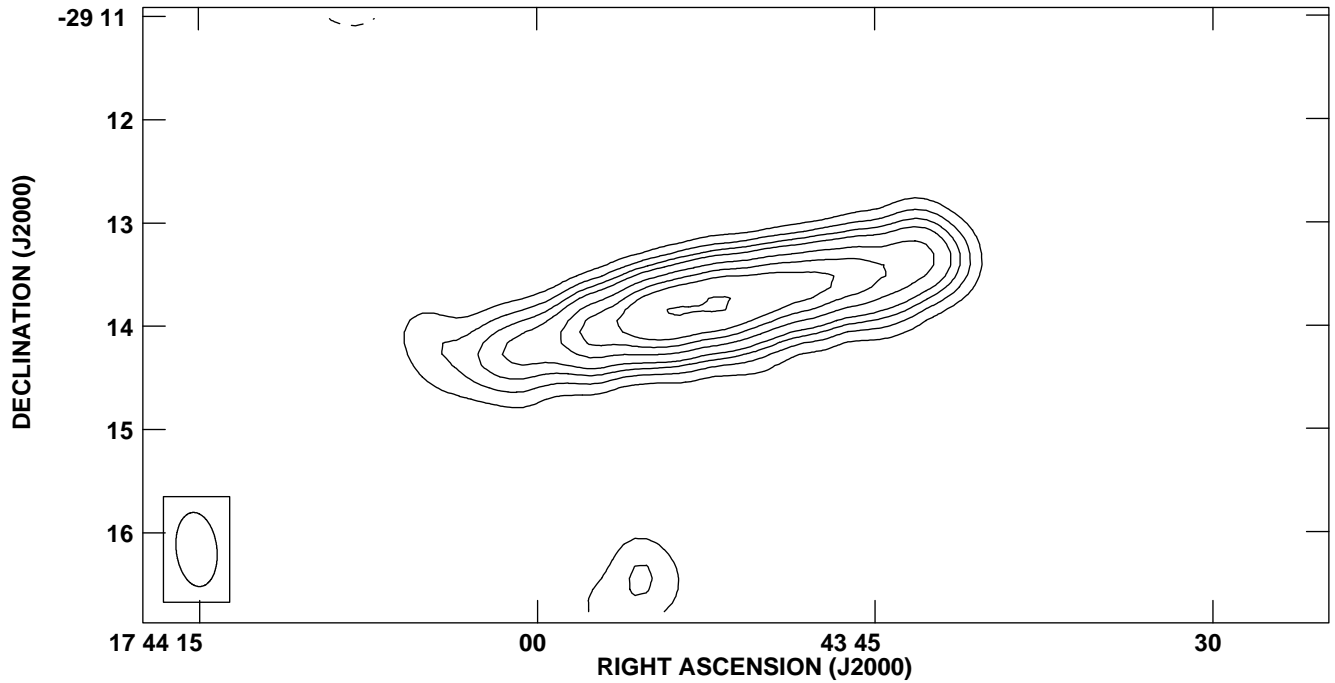


FIG. 22b

FIG. 22.—Images of the filament G359.54+0.18. (a) Gray-scale levels are linear and in units of mJy beam^{-1} . (b) Contour levels are $-15, 30, 45, 60, 75, 100, 125, 150$, and $200 \text{ mJy beam}^{-1}$. The beam is shown in the lower left.

along several of the nonthermal filaments. Although spectral index measurements are subject to errors when comparing data sets with very different observational parameters, our results for the Sgr C filament clearly indicate that the spectral index is constant with length. For the northern and

southern threads the errors are larger and do not permit a definite statement. However, within the errors the results are consistent with a constant spectral index. Our spectral indices are contrary to earlier work on the filaments, which indicated a considerable variation of spectral index with

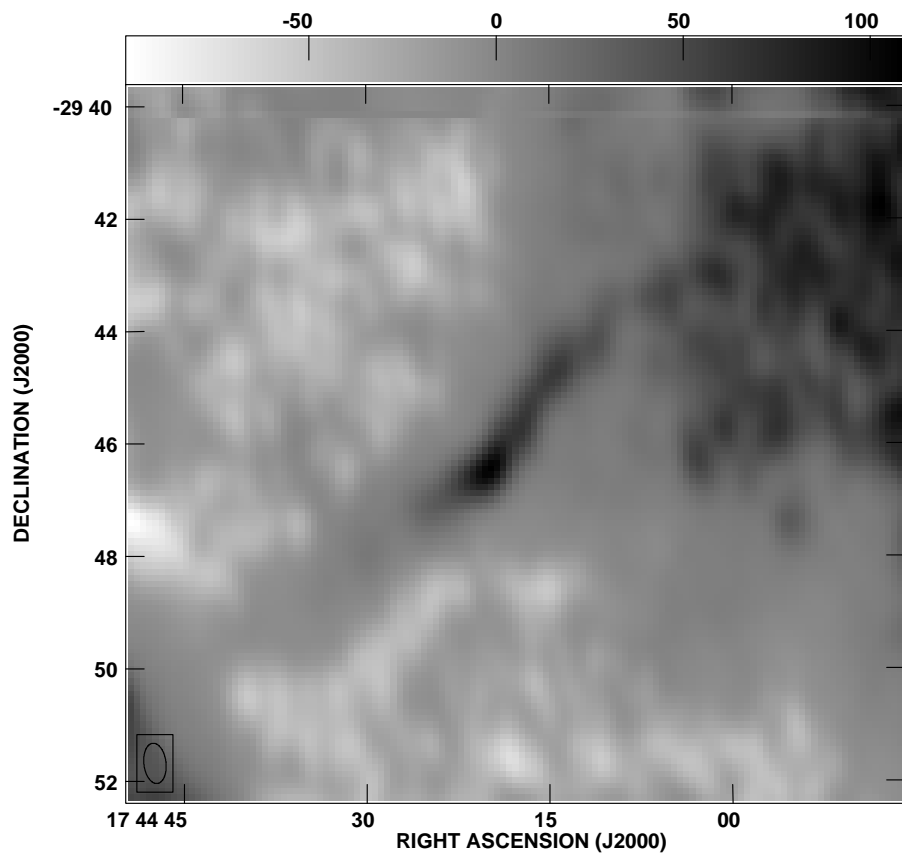


FIG. 23a

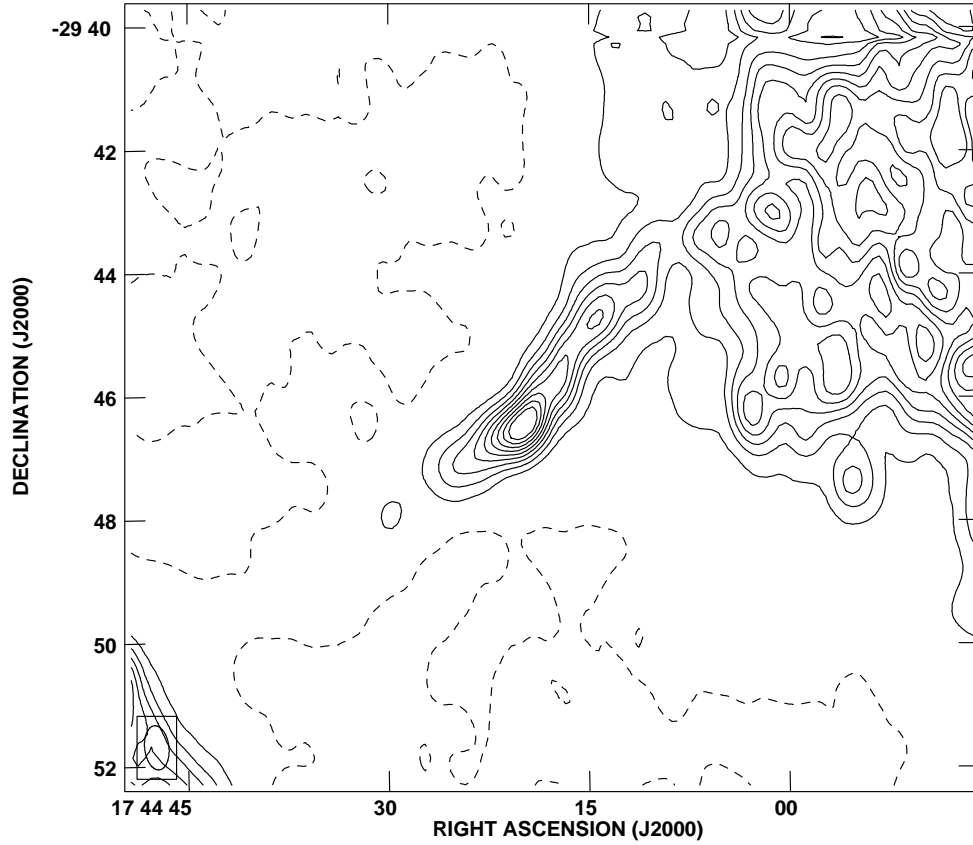


FIG. 23b

FIG. 23.—Images of the filament G359.1+0.2, the Snake. (a) Gray-scale levels are linear and in units of mJy beam⁻¹. (b) Contour levels are -20, 10, 20, 30, 40, 50, 60, 70, 80, and 90 mJy beam⁻¹. The beam is shown in the lower left.

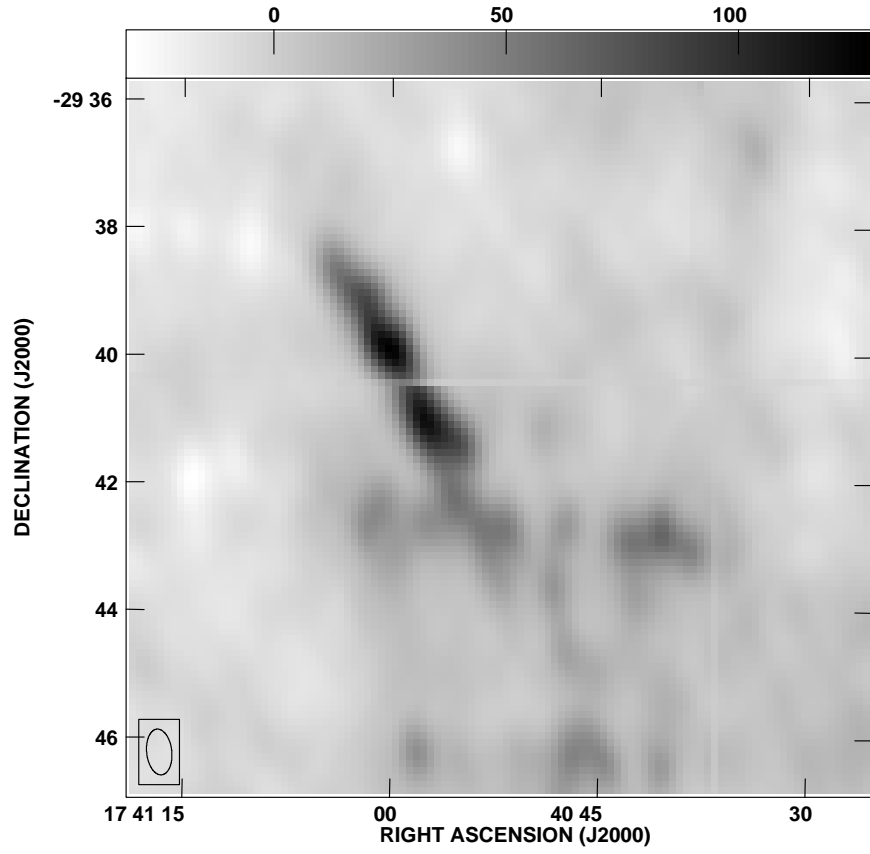


FIG. 24a

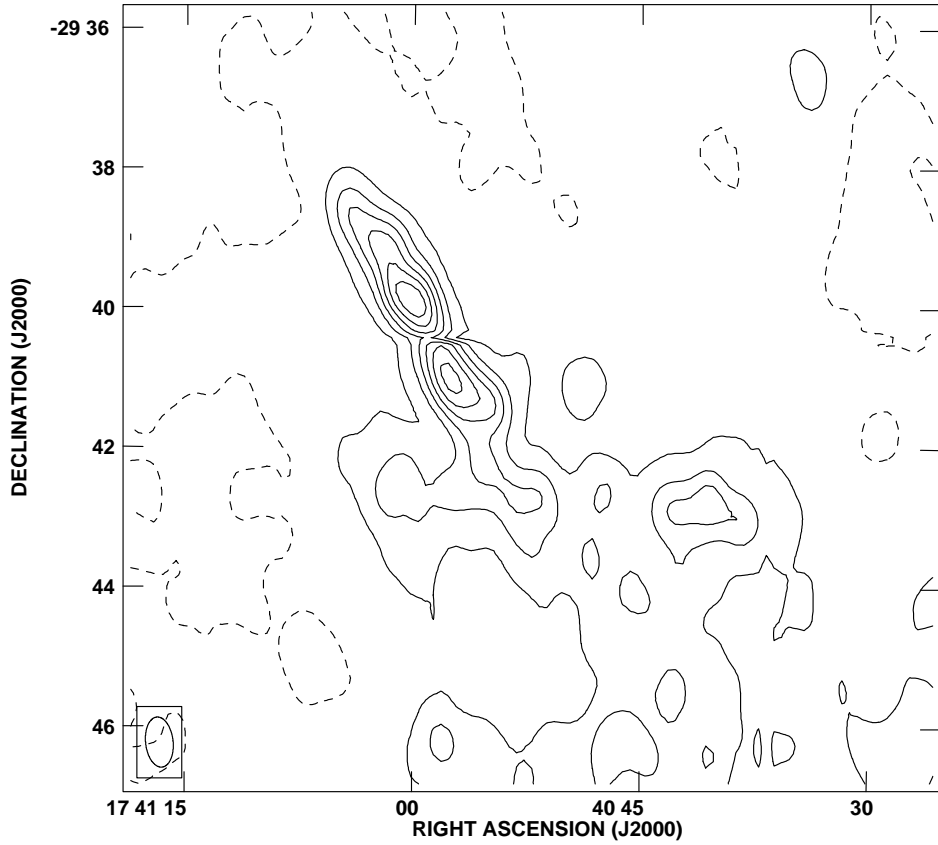


FIG. 24b

FIG. 24.—Images of the filament G358.85+0.47, the Pelican. (a) Gray-scale levels are linear and in units of mJy beam^{-1} . (b) Contour levels are $-10, 10, 30, 50, 70, 90$, and $110 \text{ mJy beam}^{-1}$. The beam is shown in the lower left.

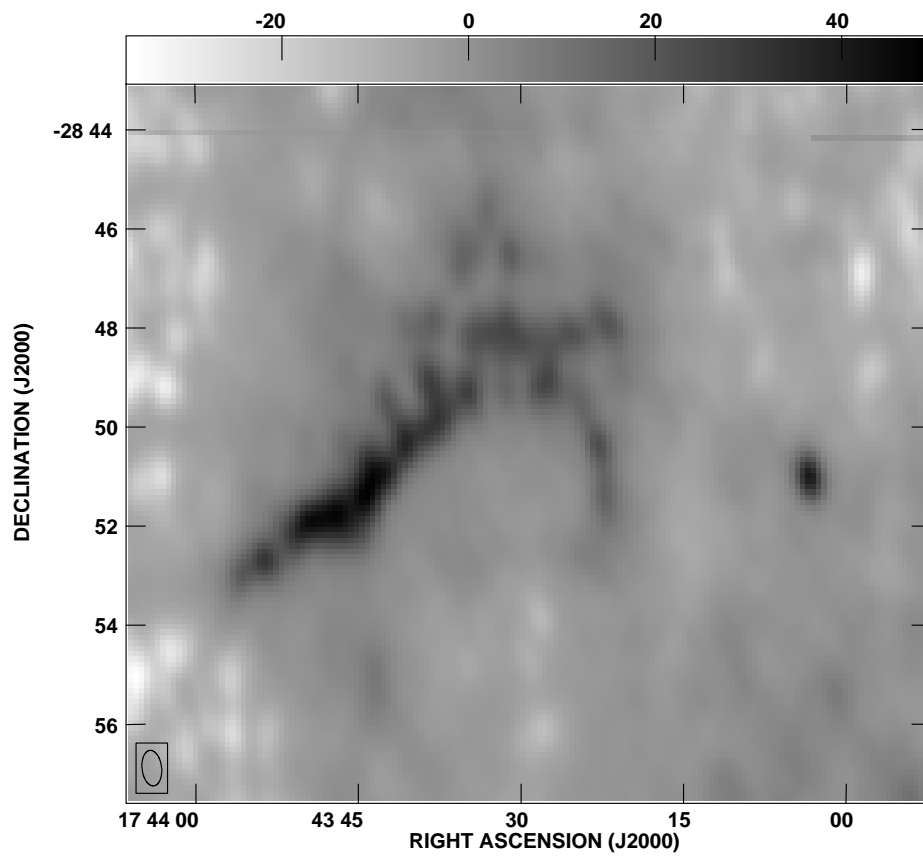


FIG. 25a

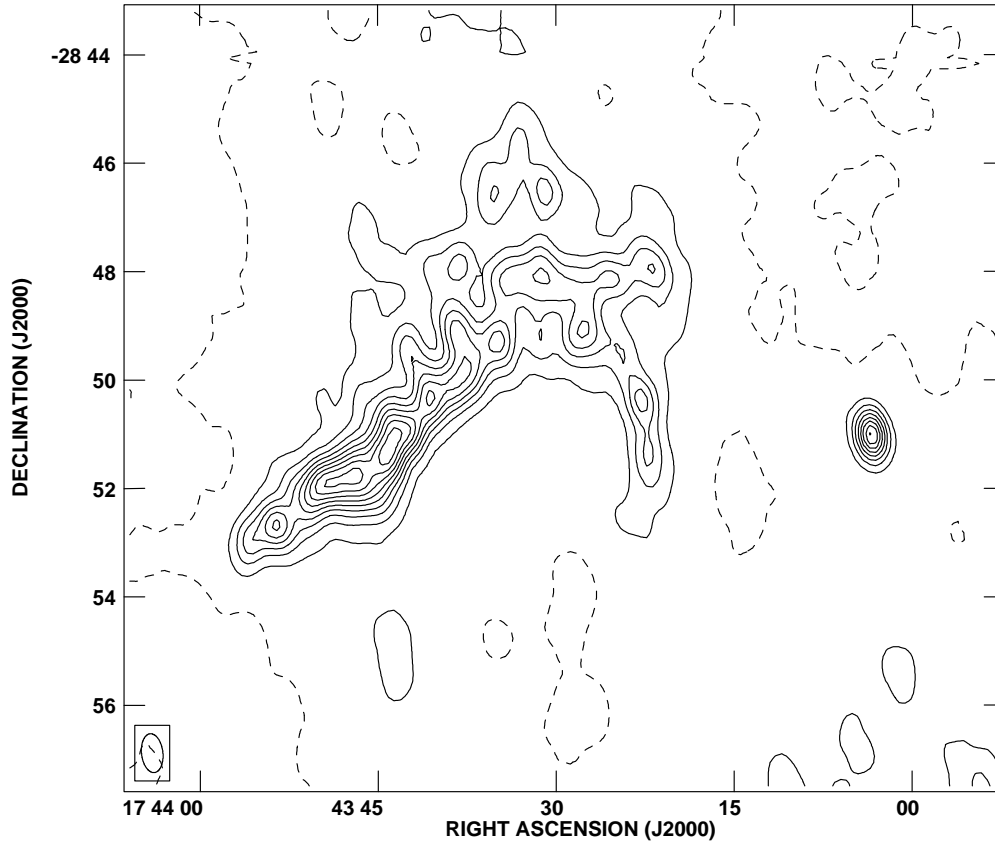


FIG. 25b

FIG. 25.—Images of G359.85+0.39, the Cane. (a) Gray-scale levels are linear and in units of mJy beam⁻¹. (b) Contour levels are -5, 5, 10, 15, 20, 25, 30, 35, 40, and 45 mJy beam⁻¹. The beam is shown in the lower left.

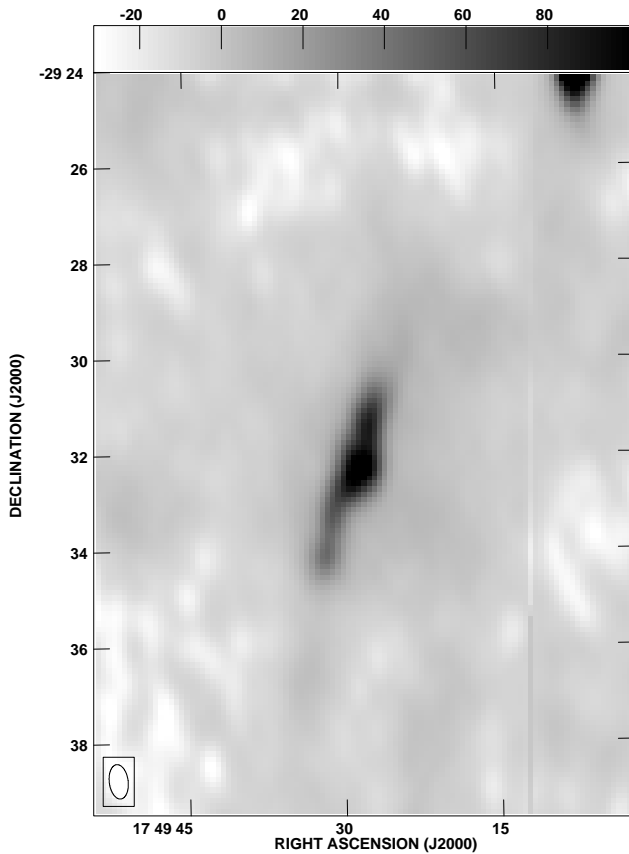


FIG. 26a

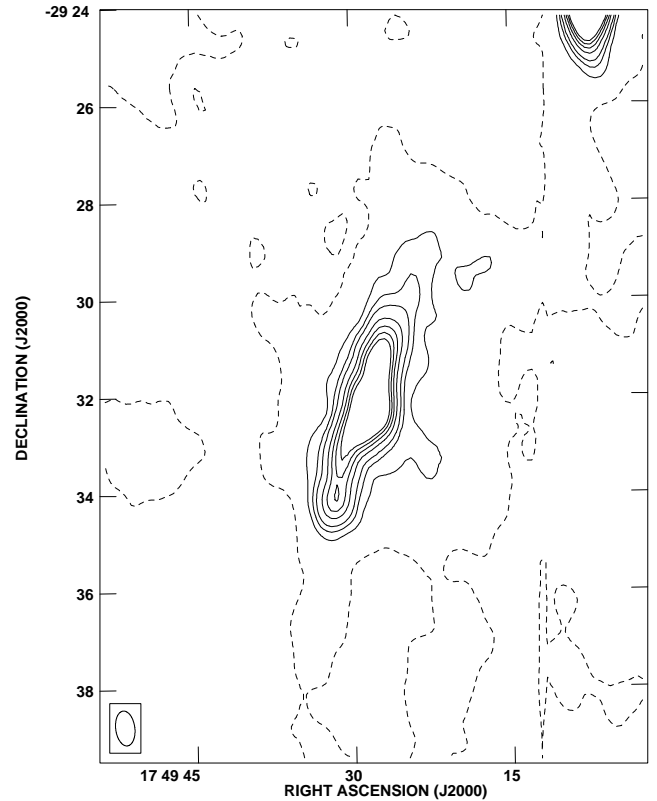


FIG. 26b

FIG. 26.—Images of G359.92–1.03. (a) Gray-scale levels are linear and in units of mJy beam^{-1} . (b) Contour levels are $-5, 5, 10, 15, 25, 35, 45$, and 55 mJy beam^{-1} . The beam is shown in the lower left.

length. The estimated synchrotron lifetime indicates there is sufficient time for the electrons to traverse the length of the filament without significant energy loss. Thus synchrotron aging may not be observed in the filaments even if the energetic electrons powering these sources are injected at one end.

We have also identified 78 small-diameter ($< 1'$) sources. These sources are concentrated toward the Galactic plane and about half of them have steep spectra ($\alpha \approx -0.8$). These sources are probably mostly extragalactic radio sources, though a small population of radio pulsars and young or distant supernova remnants cannot be excluded. The other half of the sources, for which we do not have any spectra, are significantly more concentrated toward the plane than the nonthermal sources and are thus probably H II regions.

A second epoch of Galactic center observations that includes both 74 and 330 MHz observations has recently been obtained. In addition to clarifying further the non-thermal emission from the GC, these observations will be combined with those reported here to assess source variability toward the GC.

Figure 1, subimages of many of the extended sources, and other information can be obtained via the World Wide Web.³

We thank A. Pedlar for the original VLA data on which this work is based. We thank C. Lang and H. Liszt for generously sharing their 20 cm images, which were used to estimate spectral indices for several of the NTFs. We acknowledge J. Imamura and S. Bollinger for their assistance with the figures and the small-diameter source measurements, respectively. We also thank K. Anantharamaiah for ongoing discussions concerning Galactic center work. Lastly, we thank Farhad Yusef-Zadeh, the referee, for comments that improved the paper. T. N. L. was supported by the NAVY-ASEE summer faculty program and a NASA JOVE grant to Kennesaw State University. S. D. H. was supported by a grant from the Jeffress Memorial Trust. Basic research in radio astronomy at the NRL is supported by the Office of Naval Research.

³ At <http://rsd-www.nrl.navy.mil/7213/lazio/GC/>.

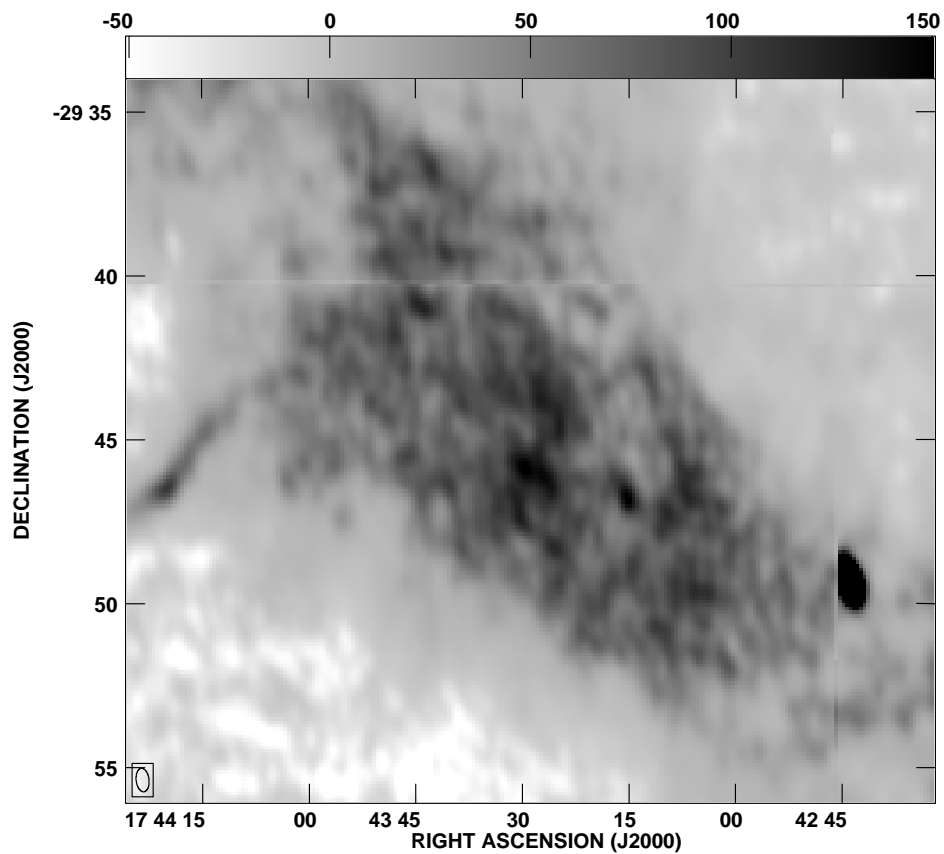


FIG. 27a

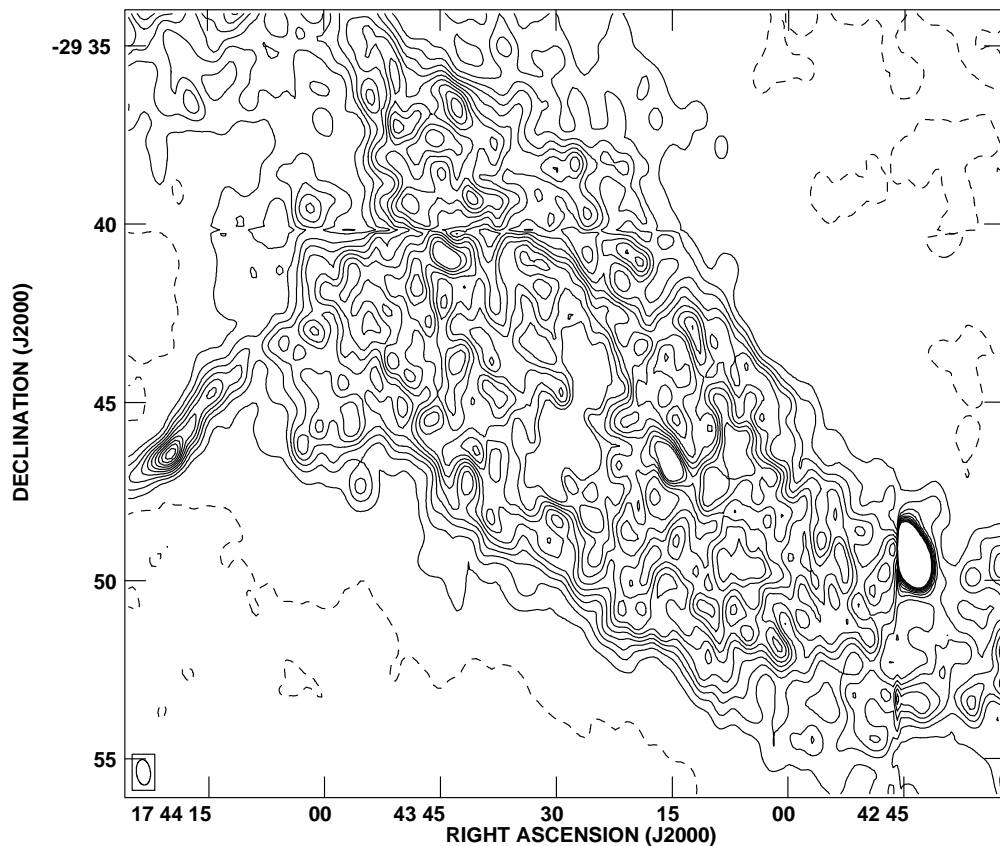


FIG. 27b

FIG. 27.—Images of the diffuse source G359.07+0.02. (a) Gray-scale levels are linear and in units of mJy beam^{-1} . (b) Contour levels are $-10, 10, 20, 30, 40, 50, 60, 70, 80, 90,$ and $100 \text{ mJy beam}^{-1}$. The beam is shown in the lower left.

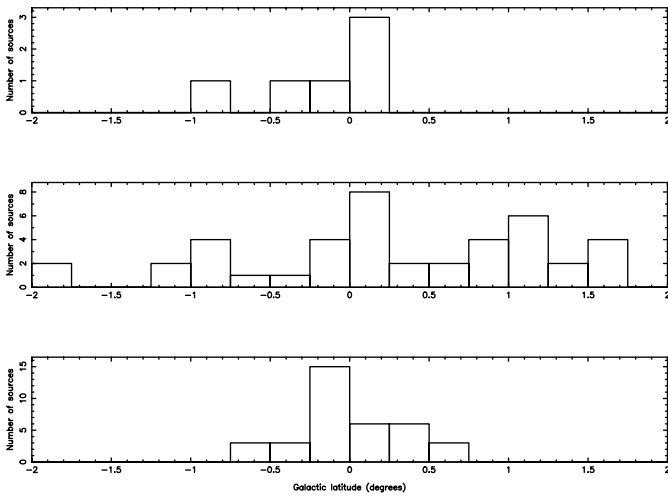


FIG. 28.—Histogram of the Galactic latitudes of the small-diameter sources. *Top*: Distribution for sources with thermal spectral indices $\alpha > -0.25$. *Middle*: Distribution for sources with nonthermal spectral indices $\alpha < -0.25$. *Bottom*: The distribution for sources with unknown spectral indices.

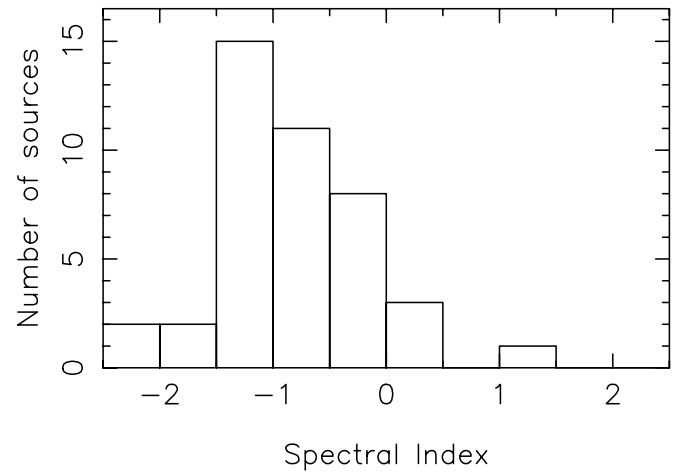


FIG. 29.—Histogram of the spectral indices between 20 and 90 cm for those small-diameter sources having NVSS counterparts.

REFERENCES

- Anantharamaiah, K. R., Lang, C. C., Kassim, N. E., Lazio, T. J. W., & Goss, W. M. 1999, in ASP Conf. Ser. 186, *The Central Parsecs of the Galaxy*, ed. H. Falcke, A. Cotera, W. J. Duschl, F. Melia, & M. J. Rieke (San Francisco: ASP), 507
- Anantharamaiah, K. R., Pedlar, A., Ekers, R. D., & Goss, W. M. 1991, *MNRAS*, 249, 262
- Balick, B., & Brown, R. L. 1974, *ApJ*, 194, 265
- Bally, J., & Yusef-Zadeh, F. 1989, *ApJ*, 336, 173
- Becker, R. H., White, R. L., Helfand, D. J., & Zoonematkermani, S. 1994, *ApJS*, 91, 347
- Becker, R. H., White, R. L., McLean, B. J., Helfand, D. J., & Zoonematkermani, S. 1990, *ApJ*, 358, 485
- Beckert, T., Duschl, W. J., Mezger, P. G., & Zylka, R. 1996, *A&A*, 307, 450
- Benford, G. 1988, *ApJ*, 333, 73
- Bridle, A. H., & Schwab, F. R. 1988, in ASP Conf. Ser. 6, *Synthesis Imaging in Radio Astronomy*, ed. R. A. Perley, F. R. Schwab, & A. H. Bridle (San Francisco: ASP), 247
- Condon, J. J., Cotton, W. D., Greisen, E. W., Yin, Q. F., Perley, R. A., Taylor, G. B., & Broderick, J. J. 1998, *AJ*, 115, 1693
- Cornwell, T. J., & Perley, R. A. 1992, *A&A*, 261, 353
- Douglas, J. N., Bash, F. N., Bozayan, F. A., Torrence, G. W., & Wolfe, C. 1996, *AJ*, 111, 1945
- Duncan, A. R., Haynes, R. F., Reich, W., Reich, P., & Gray, A. D. 1998, *MNRAS*, 299, 942
- Ekers, R. D., van Gorkom, J. H., Schwarz, U. J., & Goss, W. M. 1983, *A&A*, 122, 143
- Frail, D. A., Goss, W. M., Reynoso, E. M., Giacani, E. B., Green, A. J., & Otrupcek, R. 1996, *AJ*, 111, 1651
- Gaensler, B. M. 1998, *ApJ*, 493, 781
- Gray, A. D. 1994a, *MNRAS*, 270, 822
- 1994b, *MNRAS*, 270, 861
- Gray, A. D., Cran, L. E., Ekers, R. D., & Goss, W. M. 1991, *Nature*, 353, 237
- Gray, A. D., Nicholls, J., Ekers, R. D., & Cram, L. E. 1995, *ApJ*, 448, 164
- Helfand, D. J., & Becker, R. H. 1987, *ApJ*, 316, 616
- Kassim, N. E., Briggs, D. A., & Foster, R. S. 1998, in IAU Symp. 179, *New Horizons in Multi-Wavelength Sky Surveys*, ed. B. J. McClean (Dordrecht: Kluwer), 89
- Kassim, N. E., & Frail, D. A. 1996, *MNRAS*, 283, L51
- Kassim, N. E., LaRosa, T. N., Lazio, T. J. W., & Hyman, S. 1999, in ASP Conf. Ser. 186, *The Central Parsecs of the Galaxy*, ed. H. Falcke, A. Cotera, W. J. Duschl, F. Melia, & M. J. Rieke (San Francisco: ASP), 403
- Khokhlov, A., & Melia, F. 1996, *ApJ*, 457, L61
- Lacy, J. H., Achetermann, J. M., & Serabyn, E. 1991, *ApJ*, 380, L71
- Lang, C. C., Anantharamaiah, K. R., Kassim, N. E., & Lazio, T. J. W. 1999a, *ApJ*, 521, L41
- Lang, C. C., Morris, M., & Echevarria, L. 1999b, *ApJ*, 526, 727
- LaRosa, T. N., & Kassim, N. E. 1985, *ApJ*, 299, L13
- Lazio, T. J. W., Anantharamaiah, K. R., Goss, W. M., Kassim, N. E., & Cordes, J. M. 1999, *ApJ*, 515, 196
- Lazio, T. J. W., & Cordes, J. M. 1998, *ApJ*, 505, 715
- Lesch, H., & Reich, W. 1992, *A&A*, 264, 493
- Liszt, H. S. 1985, *ApJ*, 298, L281
- 1992, *ApJS*, 82, 495
- Liszt, H., & Spiker, R. 1995, *ApJS*, 98, 259
- Little, A. G. 1974, in IAU Symp. 60, *Galactic Radio Astronomy*, ed. F. J. Kerr & S. C. Simonson III (Dordrecht: Reidel), 491
- Lo, K. Y., & Claussen, M. J. 1983, *Nature*, 306, 647
- Mehring, D. M., Goss, W. M., Lis, D. C., Palmer, P., & Menten, K. M. 1998, *ApJ*, 493, 274
- Mereghetti, S., Sidoli, L., & Israel, G. L. 1998, *A&A*, 331, L77
- Mezger, P. G., Duschl, W. J., & Zylka, R. 1996, *A&A Rev.*, 7, 289
- Mezger, P. G., Zylka, R., Salter, C. J., Wink, J. E., Chini, R., Kreysa, E., & Tufts, R. 1989, *A&A*, 209, 337
- Morris, M. 1994, in *The Nuclei of Normal Galaxies: Lessons from the Galactic Center*, ed. R. Genzel & A. I. Harris (Dordrecht: Kluwer), 185
- 1996, in IAU Symposium 169, *Unsolved Problems of the Milky Way*, ed. L. Blitz & P. Teuben (Dordrecht: Kluwer), 247
- Morris, M., & Serabyn, E. 1996, *ARA&A*, 34, 645
- Morris, M., & Yusef-Zadeh, F. 1985, *AJ*, 90, 2511
- Pauls, T., & Mezger, P. G. 1975, *A&A*, 44, 259
- Pedlar, A., Anantharamaiah, K. R., Ekers, R. D., Goss, W. M., van Gorkom, J. H., Schwarz, U. J., & Zhao, J.-H. 1989, *ApJ*, 342, 769
- Reich, W., & Fürst, E. 1984, *A&AS*, 57, 165
- Reich, W., Sofue, Y., & Fürst, E. 1987, *PASJ*, 39, 573
- Reynolds, S. P. 1988, in *Galactic and Extragalactic Radio Astronomy*, ed. G. L. Verschuur & K. I. Kellermann (Berlin: Springer-Verlag), 439
- Serabyn, E., Lacy, J. H., Townes, C. H., & Bharat, R. 1988, *ApJ*, 326, 171
- Serabyn, E., & Morris, M. 1994, *ApJ*, 424, L91
- Shore, S. N., & LaRosa, T. N. 1999, *ApJ*, 521, 587
- Sofue, Y. 1985, *PASJ*, 37, 697
- 1994, *ApJ*, 431, L91
- Sofue, Y., & Handa, T. 1984, *Nature*, 310, 568
- Sofue, Y., Reich, W., & Reich, P. 1989, *ApJ*, 341, L47
- Staguhn, J., Stutski, J., Uchida, K. I., & Yusef-Zadeh, F. 1998, *A&A*, 336, 290
- Stewart, R. T., Haynes, R. F., Gray, A. D., & Reich, W. 1994, *ApJ*, 432, L39
- Terzan, A., & Gosset, E. 1991, *A&AS*, 90, 451
- Uchida, K. I., Morris, M., Bally, J., Pound, M., & Yusef-Zadeh, F. 1992a, *ApJ*, 398, 128
- Uchida, K. I., Morris, M., Serabyn, E., & Gusten, R. 1996, *ApJ*, 462, 768
- Uchida, K., Morris, M., & Yusef-Zadeh, F. 1992b, *AJ*, 104, 1533
- Uchida, Y., & Shibata, K. 1986, *PASJ*, 38, 631
- Uchida, Y., Shibata, K., & Sofue, Y. 1985, *Nature*, 317, 699
- Wentzel, D. G. 1974, *ARA&A*, 12, 71
- Yusef-Zadeh, F. 1989a, *ApJ*, 343, 703
- 1989b, in IAU Symposium 136, *The Center of the Galaxy*, ed. M. Morris (Dordrecht: Kluwer), 243

- Yusef-Zadeh, F., & Bally, J. 1989, in IAU Symposium 136, The Center of The Galaxy, ed. M. Morris (Dordrecht: Kluwer), 197
- Yusef-Zadeh, F., Goss, W. M., Roberts, D. A., Robinson, B., & Frail, D. A. 1999, ApJ, 527, 172
- Yusef-Zadeh, F., & Morris, M. 1987a, ApJ, 322, 721
- . 1987b, AJ, 94, 1128
- Yusef-Zadeh, F., Morris, M., & Chance, D. 1984, Nature, 310, 557
- Yusef-Zadeh, F., Wardle, M., & Parastaran, P. 1997, ApJ, 475, L119
- Yusef-Zadeh, F. 1999, in ASP Conf. Ser. 186, The Central Parsecs of the Galaxy, ed. H. Falcke, A. Cotera, W. J. Duschl, F. Melia, & M. J. Rieke (San Francisco: ASP)
- Zoonematkermani, S., Helfand, R. H., Becker, R. H., White, R. L., & Perley, R. A. 1990, ApJS, 74, 181

ERRATUM: “A WIDE-FIELD 90 CENTIMETER VLA IMAGE OF THE GALACTIC CENTER REGION”
[ASTRON. J. 119, 207 (2000)]

T. N. LAROSA

Department of Biological and Physical Sciences, Kennesaw State University

NAMIR E. KASSIM AND T. JOSEPH W. LAZIO

Remote Sensing Division, Naval Research Laboratory

AND

S. D. HYMAN

Department of Physics, Sweet Briar College

Received 2000 February 25; accepted 2000 March 10

We inadvertently failed to acknowledge that the VLA is operated by the National Radio Astronomy Observatory, which is a facility of the National Science Foundation operated under cooperative agreement by Associated Universities, Inc.